



OPEN

Neutrophils incite and macrophages avert electrical storm after myocardial infarction

Jana Grune^{1,2}, Andrew J. M. Lewis^{1,2,23}, Masahiro Yamazoe^{1,2,23}, Maarten Hulsmans^{ID 1,2}, David Rohde^{ID 1,2}, Ling Xiao^{ID 3}, Shuang Zhang^{1,2}, Christiane Ott^{ID 4,5}, David M. Calcagno^{ID 6}, Yirong Zhou^{1,7}, Kerstin Timm^{ID 8}, Mayoaran Shanmuganathan^{ID 9,10}, Fadi E. Pulous^{ID 1,2}, Maximilian J. Schloss^{1,2}, Brody H. Foy^{1,11}, Diane Capen¹², Claudio Vinegoni^{ID 1,2}, Gregory R. Wojtkiewicz^{ID 1}, Yoshiko Iwamoto¹, Tilman Grune^{4,5}, Dennis Brown¹², John Higgins^{ID 1,11}, Vanessa M. Ferreira⁹, Neil Herring^{ID 10,13}, Keith M. Channon^{9,10}, Stefan Neubauer^{9,10}, Oxford Acute Myocardial Infarction (OxAMI) Study*, David E. Sosnovik^{3,14,15}, David J. Milan¹⁶, Filip K. Swirski^{ID 17}, Kevin R. King^{6,18}, Aaron D. Aguirre^{ID 1,7,15}, Patrick T. Ellinor^{ID 3,15,19} and Matthias Nahrendorf^{ID 1,2,20}

Sudden cardiac death, arising from abnormal electrical conduction, occurs frequently in patients with coronary heart disease. Myocardial ischemia simultaneously induces arrhythmia and massive myocardial leukocyte changes. In this study, we optimized a mouse model in which hypokalemia combined with myocardial infarction triggered spontaneous ventricular tachycardia in ambulatory mice, and we showed that major leukocyte subsets have opposing effects on cardiac conduction. Neutrophils increased ventricular tachycardia via lipocalin-2 in mice, whereas neutrophilia associated with ventricular tachycardia in patients. In contrast, macrophages protected against arrhythmia. Depleting recruited macrophages in *Ccr2*^{-/-} mice or all macrophage subsets with *Csf1* receptor inhibition increased both ventricular tachycardia and fibrillation. Higher arrhythmia burden and mortality in *Cd36*^{-/-} and *Mertk*^{-/-} mice, viewed together with reduced mitochondrial integrity and accelerated cardiomyocyte death in the absence of macrophages, indicated that receptor-mediated phagocytosis protects against lethal electrical storm. Thus, modulation of leukocyte function provides a potential therapeutic pathway for reducing the risk of sudden cardiac death.

Sudden cardiac death occurs when the normal rhythmic depolarization of the myocardium is interrupted, stopping the delivery of oxygenated blood. This condition, which occurs more than 200,000 times in the United States and over 5 million times globally per year, has a survival rate below 10%¹. The most prevalent underlying pathology is myocardial ischemia, which triggers ventricular tachycardia (VT) or ventricular fibrillation (Vfib). If these arrhythmias are not rapidly treated, then death ensues. Despite this prevalence and lethality, current treatment options are largely limited to defibrillation, which restores normal myocyte depolarization. If a patient survives, secondary prevention relies on improving blood flow and implanting a defibrillator. Although implantable defibrillators can reduce future cardiac mortality, they do not prevent

recurrent arrhythmias, and device therapy can impair quality of life. Because it is difficult to predict arrhythmia risk, one-third of patients with a defibrillator never receive an appropriate therapy².

The fundamental electrophysiological mechanisms leading to ventricular arrhythmias have been extensively studied. After myocardial infarction (MI), the normal homogeneous depolarization of the myocardium is replaced by areas of regional heterogeneity that serve as the substrate for re-entry³. Various pathologies can propagate re-entry, including abnormal ion channel function⁴, structural changes in ion channels and gap junctions due to oxidation⁵ and genetic disorders. Myocardial fibrosis and dying or dead cells may also slow conduction and, thus, contribute to the arrhythmogenic substrate⁶.

¹Center for Systems Biology, Massachusetts General Hospital and Harvard Medical School, Boston, MA, USA. ²Department of Radiology, Massachusetts General Hospital and Harvard Medical School, Boston, MA, USA. ³Cardiovascular Research Center, Massachusetts General Hospital and Harvard Medical School, Boston, MA, USA. ⁴DZHK (German Centre for Cardiovascular Research), Partner Site Berlin, Berlin, Germany. ⁵Department of Molecular Toxicology, German Institute of Human Nutrition Potsdam-Rehbruecke (DIFe), Nuthetal, Germany. ⁶Department of Bioengineering, University of California, San Diego, La Jolla, CA, USA. ⁷Wellman Center for Photomedicine, Massachusetts General Hospital and Harvard Medical School, Boston, MA, USA. ⁸Department of Pharmacology, University of Oxford, Oxford, UK. ⁹Radcliffe Department of Medicine, University of Oxford, Oxford, UK. ¹⁰National Institute for Health (NIHR) Biomedical Research Centre, Oxford University Hospitals NHS Foundation Trust, John Radcliffe Hospital, Oxford, UK. ¹¹Department of Pathology, Massachusetts General Hospital, Boston, MA, USA. ¹²Program in Membrane Biology, Nephrology Division, Department of Medicine, Massachusetts General Hospital and Harvard Medical School, Boston, MA, USA. ¹³Department of Physiology, Anatomy and Genetics, University of Oxford, Oxford, UK. ¹⁴Martinos Center for Biomedical Imaging, Massachusetts General Hospital and Harvard Medical School, Boston, MA, USA. ¹⁵Division of Cardiology, Massachusetts General Hospital, Harvard Medical School, Boston, MA, USA. ¹⁶Leducq Foundation, Boston, MA, USA. ¹⁷Cardiovascular Research Institute and Department of Medicine, Icahn School of Medicine at Mount Sinai, New York, NY, USA. ¹⁸Department of Medicine, Division of Cardiovascular Medicine, University of California, San Diego La Jolla, CA, USA. ¹⁹The Broad Institute of MIT and Harvard, Cambridge, MA, USA. ²⁰Department of Internal Medicine, University Hospital Wuerzburg, Wuerzburg, Germany. ²³These authors contributed equally and are listed in alphabetical order: Andrew J. M. Lewis, Masahiro Yamazoe. *A list of authors and their affiliations appears at the end of the paper. e-mail: mnahrendorf@mgh.harvard.edu

The emerging importance of innate immune cells in the healthy and ischemic heart raises the possibility that leukocytes may contribute to rhythm disorders or help to prevent arrhythmias. Cardiac resident macrophages, with a frequency of 6–8% in the mouse and human heart^{7,8}, support normal electrical conduction⁹ and are essential for myocyte energy metabolism¹⁰. Conditions that increase the risk of an arrhythmia, such as acute MI or myocarditis, are associated with massive changes in myocardial leukocyte numbers and phenotypes¹¹.

Given that leukocytes frequently modulate stromal cell and organ functions, we explored, in this study, their contribution to ventricular arrhythmia, a prevalent condition with an unmet therapeutic need. A substantial hurdle for such studies is the dearth of suitable animal models. Although large animals readily develop spontaneous arrhythmia, tools for studying their immune system are limited. By contrast, the mouse offers a plethora of well-developed methods; however, spontaneous VT and Vfib rarely occur. The high heart rate, the small size and distinct action potential have been discussed as reasons for the lack of spontaneous VT¹². We overcame this challenge with a clinically relevant and surprisingly simple intervention: diet-induced hypokalemia preceding ischemia, which gave rise to recurrent ventricular arrhythmias in conscious, ambulatory mice. With this tool in hand, we then canvassed the contribution of leukocytes to ventricular arrhythmia, starting with neutrophils and macrophages—the most abundant immune cells in the heart.

Results

A mouse model of electrical storm. Patients with acute MI may develop hypokalemia with serum potassium levels below 3.5 mM due to treatment with diuretics or activation of the sympathetic nervous system¹³. Because the prevalence of life-threatening tachyarrhythmias is inversely correlated to serum potassium levels¹³, we hypothesized that hypokalemic mice develop spontaneous arrhythmias after MI. We tested this hypothesis by feeding C57BL/6J wild-type mice a potassium-deficient diet. Implantation of a telemetric device allowed us to monitor awake mice after infarct induction (Fig. 1a). Providing a potassium-deficient diet for 3 weeks established moderate hypokalemia with accompanying electrolyte disturbances (Fig. 1b and Extended Data Fig. 1a,b). Hypokalemia reduced the resting heart rate and prolonged the QTc time, indicating slower ventricular repolarization (Extended Data Fig. 1c,d). The diastolic and systolic functions as measured by echocardiography were unaltered (Extended Data Fig. 1e,f). Hypokalemia did not affect neutrophil and monocyte recruitment after MI, resident cardiac macrophage disappearance from the ischemic myocardium or infarct size 24 hours after permanent coronary artery ligation (Fig. 1c–e and Extended Data Fig. 1g).

Only occasional ventricular extrasystoles were detected in hypokalemic mice without MI and normokalemic mice with MI, but Spontaneous Tachycardia Occurred frequently in hypokalemic mice with Myocardial infarction (in the following referred to as STORM; Fig. 1f,g). VT was particularly common during the first day after MI, and most episodes occurred during the first 8 hours (Fig. 1h), a timeline that mirrors the clinical situation^{14,15}. VT burden inter-observer variability analysis showed an acceptable bias of 4.2% (Extended Data Fig. 1h). In STORM mice, VT and Vfib reached an incidence of 90% and 31%, respectively (Fig. 1i). The average VT burden of STORM mice was greater than 10,000 cardiac cycles, which translates to over 12 minutes of ventricular arrhythmia (Fig. 1i). Given this prevalence and time course, the VT burden proved a particularly instructive metric in our subsequent studies. Compared to the regular sinus rhythm of STORM mice, the heart rate during VT episodes was twice as fast, well above 1,000 beats per minute (Fig. 1j). STORM mice and normokalemic MI mice had similar survival during the first 24 hours after MI, suggesting that sudden cardiac death is not frequent in wild-type STORM mice

(Fig. 1k). Of note, MI carries considerable mortality in mice; however, this mostly takes place several days later¹⁶.

When we induced VT by rapid pacing in anesthetized mice, arrhythmias were observed in hypokalemic mice without MI and in normokalemic mice with MI. This procedure could not be completed in STORM mice due to frequent recurrent episodes of spontaneous VT, which proved lethal under anesthesia (Extended Data Fig. 1l–k). The arrhythmia burden was similar in male and female STORM mice (Extended Data Fig. 1l,m). In sum, STORM represents a robust model of spontaneous ventricular arrhythmia in awake wild-type mice. We then sought to use the STORM model to investigate the role of key leukocyte populations in arrhythmogenesis.

Neutrophils incite ventricular arrhythmia. We began by investigating neutrophils, which accumulate in the infarct within minutes of ischemia onset and reach their peak abundance 24 hours later¹¹. The diverse roles of neutrophils after MI have been described in great detail, but it remains unclear whether they contribute to ventricular arrhythmias. Hence, we depleted circulating neutrophils with antibody injections against neutrophil surface markers (Fig. 2a) ¹⁷. To exclude the effects of neutrophil depletion on infarct size, which influences the occurrence of arrhythmia¹⁸, we opted for permanent coronary artery occlusion without re-perfusion. Antibody treatment sufficiently depleted neutrophils in STORM mice, whereas monocyte and macrophage populations, blood troponin, 24-hour infarct size and heart weight remained unaffected (Fig. 2a–c and Extended Data Fig. 2a–c). Notably, neutrophil depletion lowered the VT burden when compared to STORM mice with regular neutrophil counts, indicating that neutrophils promote ventricular arrhythmias (Fig. 2d–f and Extended Data Fig. 2d). Neutrophil depletion did not affect the repolarization parameter QTc time (Extended Data Fig. 2e).

To investigate whether neutrophils accumulate in myocardial areas with disturbed conduction, we applied intravital microscopy to beating Langendorff-perfused hearts from *Myh6-GCaMP8* mice (Fig. 2g). *Myh6-GCaMP8* mice express a sensitive Ca²⁺ indicator GCaMP8 under control of the cardiomyocyte-specific *Myh6* promoter, which increases green fluorescent protein (GFP) signal when cytosolic calcium binds to GCaMP8 during systole. ECG-gated imaging of paced isolated hearts focused on the infarct border zone, which we identified with fluorescent beads indicating blood flow (Fig. 2h,i). In every location, we recorded a time-lapse series in which each image frame covered the same portion of the cardiac cycle. We compared these temporal data points to each other by generating a fluorescence intensity standard deviation map (Fig. 2j–l). In *Myh6-GCaMP8* mice without MI, this procedure resulted in homogeneously low standard deviation values across the field of view (FOV), given that all cardiomyocytes cycled synchronously (Extended Data Fig. 2f). In contrast, in mice with MI, we detected regional Ca²⁺ signal inhomogeneity, revealing myocytes in which the timing of peak cytosolic Ca²⁺ concentrations differed from surrounding cells and shifted from cycle to cycle (Fig. 2j–l and Supplementary Videos 1 and 2). Merging standard deviation maps (which we considered ‘dyssynchrony’ maps) with a spectrally resolved acquisition channel reporting on Ly6G⁺ neutrophils, we explored the regional association of neutrophils with dyssynchronous cardiomyocytes. Neutrophils assembled in the vicinity of dyssynchronous cardiomyocytes, whereas randomly placed spots showed no such association (Fig. 2m,n and Extended Data Fig. 2g), implicating neutrophil proximity to heterogeneously depolarizing cardiomyocytes.

To assess the relevance of neutrophils in the clinical setting, we first retrospectively studied patients with ST-elevation myocardial infarction (STEMI) who underwent primary percutaneous coronary intervention (PPCI) and subsequent continuous ECG monitoring for up to 48 hours at Oxford University Hospitals ($n=217$,

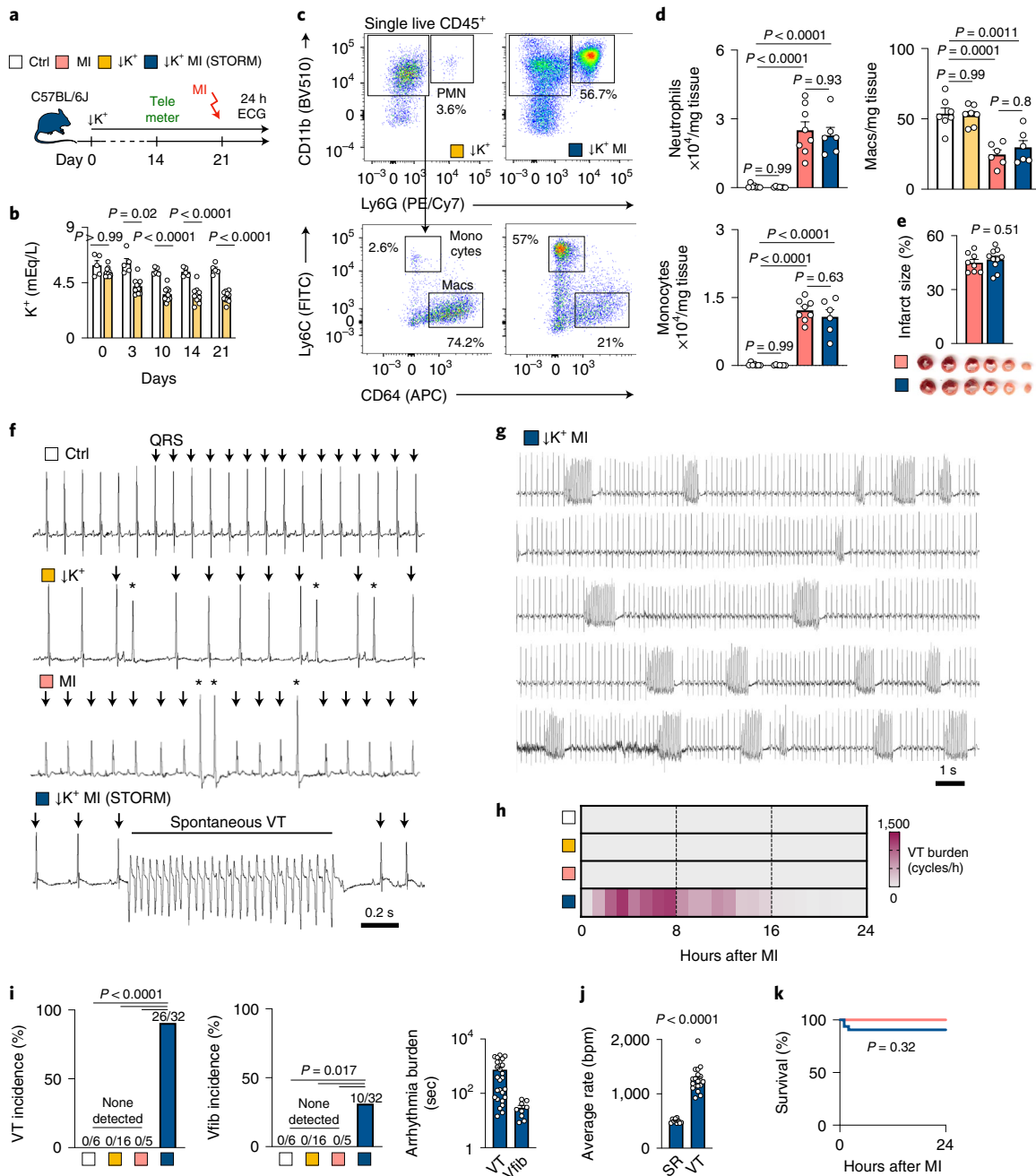


Fig. 1 | A mouse model of spontaneous electrical storm. **a**, Experimental outline for electrical storm induced by hypokalemia ($\downarrow K^+$) and MI. ECG recordings are from ambulatory mice within 24 hours after MI. **b**, Plasma potassium levels in control mice ($n=5$) and mice fed a potassium-deficient diet ($n=10$). A two-way ANOVA followed by Tukey's multiple comparisons test was used for statistical analysis. **c**, Flow plots showing neutrophils (PMN), monocytes and cardiac macrophages (Macs) in hearts of hypokalemic and STORM mice. **d**, Quantification of flow cytometry for cardiac neutrophils, monocytes and macrophages in naive mice ($n=7$), hypokalemic mice ($n=7$), MI mice ($n=8$) and STORM mice 24 hours after MI ($n=6$). A one-way ANOVA followed by Tukey's multiple comparisons test was used for statistical analysis. **e**, Infarct size in normokalemic ($n=8$) and STORM ($n=10$) mice by triphenyltetrazolium chloride (TTC) staining 24 hours after MI. An unpaired two-sided t-test was used for statistical analysis. **f**, ECG from telemetric recordings in ambulatory mice. Arrows indicate regular QRS complex; asterisks indicate extrasystoles and VT ventricular tachycardia. **g**, Long ECG strip from a STORM mouse. **h**, Heat map of VT burden expressed as cardiac cycles spent in VT per hour. **i**, VT incidence, Vfib incidence and VT and Vfib burden expressed as seconds spent within 24 hours after MI. Mouse numbers are indicated in brackets. A one-sided chi-square test was used for statistical analysis. **j**, Heart rate during sinus rhythm (SR) and VT expressed as beats per minute (bpm) in STORM mice. A Mann-Whitney test was used for statistical analysis. **k**, Kaplan-Meier survival curve of mice with MI ($n=10$) and STORM ($n=32$). A two-sided log-rank Mantel-Cox test was used for statistical analysis. Data are mean \pm s.e.m.

Oxford cohort; Fig. 2o, Extended Data Fig. 2h and Extended Data Table 1). We stratified this patient cohort using a prospectively defined arrhythmia score: (i) no arrhythmias, (ii) ventricular ectopic

beats, (iii) non-sustained VT and (iv) sustained VT or Vfib. A higher circulating neutrophil count was associated with an increased risk of early VT or Vfib ($P=0.0003$ for trend across the a priori ordered

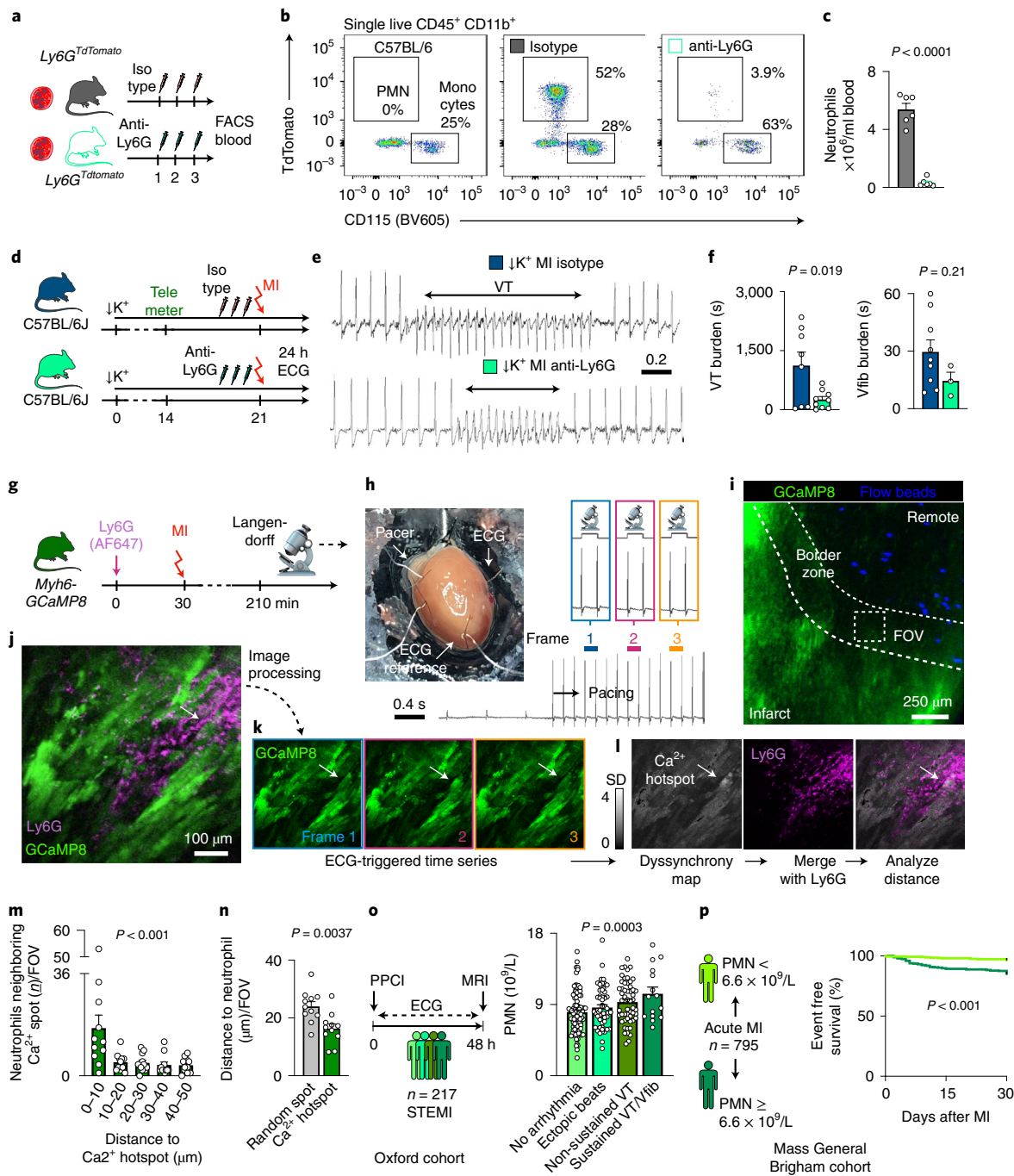


Fig. 2 | Neutrophils promote ventricular arrhythmia. **a**, Experimental outline for *Ly6G*^{TdTomato} mice with neutrophil depletion, numbers indicate days. **b**, Flow cytometry for blood neutrophils (PMN) and monocytes in *Ly6G*^{TdTomato} mice undergoing isotype or anti-*Ly6G* antibody injections. **c**, Blood neutrophil counts in isotype ($n=6$) and anti-*Ly6G* depleting antibody ($n=7$) injected mice. A two-sided unpaired *t*-test was used. **d**, Experimental outline for neutrophil depletion in STORM mice, numbers indicate days. **e**, ECG recordings in STORM mice treated with isotype or anti-*Ly6G* antibody. **f**, VT burden and Vfib burden detected during 24 hours after MI (isotype: $n=8$, anti-*Ly6G*: $n=9$). A two-sided unpaired *t*-test was used. **g**, Experimental design. Langendorff-perfused hearts from *Myh6-GCaMP8* mice were injected with anti-*Ly6G* (AF647) to label neutrophils, 3 hours after MI. **h**, Original ECG recordings indicating imaging acquisition protocol. **i**, Confocal microscopy of infarct border zone. Blood flow determination beads separate the remote from the infarct zone. Scale bar, 250 μm . **j**, Cardiomyocyte with asynchronous Ca^{2+} signal (arrow) surrounded by Ly6G⁺ neutrophils. Scale bar, 100 μm . This experiment was repeated independently four times. **k**, Time series of Ca^{2+} signal used to identify Ca^{2+} hotspots. The arrow indicates an asynchronous myocyte (see also Supplementary Video 1). **l**, Dyssynchrony map reveals asynchronous cardiomyocytes and was merged with the Ly6G channel. **m**, Distances from neutrophils to Ca^{2+} hotspots ($n=11$ FOVs from $n=3$ mice). A one-way ANOVA was used. **n**, Distance of neutrophils to a random spot (gray bar) or a Ca^{2+} hotspot (green). A two-sided unpaired *t*-test was used. **o**, Neutrophil counts from patients with STEMI and PPCI in the Oxford cohort ($n=217$) were stratified across the following groups: (i) no arrhythmia ($n=91$ patients), (ii) ventricular ectopic beats ($n=57$ patients), (iii) non-sustained VT ($n=54$ patients) and (iv) sustained VT or Vfib ($n=15$ patients). A Jonckheere-Terpstra test was used. **p**, Patients with acute MI ($n=795$, Mass General Brigham cohort) were dichotomized at the median neutrophil count and followed for a composite outcome of death or cardiac arrest. A Gehan-Breslow-Wilcoxon test was used. Data are mean \pm s.e.m. FACS, fluorescence-activated cell sorting.

groups; Fig. 2o). In a logistic regression model (Methods), a higher neutrophil count remained associated with the composite outcome of non-sustained VT, sustained VT or Vfib, even when adjusting for the acute infarct size (measured using magnetic resonance imaging (MRI)) and other factors known to alter the risk of ventricular arrhythmia after MI, including ischemic time and prior beta-blocker use (for each 1×10^9 per L increase in neutrophil count: hazard ratio (HR) = 1.20, 95% confidence interval (CI): 1.06–1.36, $P=0.003$). In a separate retrospective analysis, we studied the link between circulating neutrophils and clinical outcomes in a cohort of patients with acute MI (both STEMI and NSTEMI, $n=795$, Mass General Brigham cohort; Extended Data Fig. 2i and Extended Data Table 2), in which ventricular arrhythmia is a leading cause of death¹⁹. A high neutrophil count, dichotomized at the median of 6.6×10^9 per L for this cohort, was associated with a four-fold elevated risk of cardiac arrest or death at 30 days (HR = 4.5, 95% CI: 2.5–8.1, $P<0.001$; Fig. 2p). The association with 30-day death or cardiac arrest remained significant in a series of Cox regression analyses controlling for covariates, including age, sex, peak troponin level, monocyte count and creatinine (Extended Data Table 3). Of note, 24% of patients in the Mass General Brigham cohort experienced hypokalemia with a potassium level below 3.5 mmol L^{-1} (Extended Data Fig. 2j), indicating that the parallel observations in the STORM mouse model and in infarct patients may carry clinical relevance. Taken together, these clinical data link blood neutrophil expansion with the occurrence of ventricular arrhythmias and adverse prognosis in patients with MI, matching the causal relationship observed in the ischemic myocardium of STORM mice. However, we acknowledge that our retrospective analyses of both human cohorts are limited by potential confounding from unmeasured risk factors for ventricular arrhythmia. In the Mass General Brigham cohort, it was not possible to ascertain cardiac rhythm at the time of death; hence, non-arrhythmic causes of death are likely to have contributed to the reported outcome.

Neutrophil-derived lipocalin-2 is pro-arrhythmic. We next sought to investigate the mechanistic link between neutrophils and VT. We first tested if neutrophil depletion reduces ischemic cell death but found similar numbers of TUNEL⁺ myocytes and caspase-3 activity in the infarcts of STORM mice with reduced and normal neutrophil counts at a time when arrhythmia was most prevalent (Extended Data Fig. 2k,l). We then explored whether neutrophils promote post-MI arrhythmia via reactive oxygen species (ROS)²⁰. Five hours after coronary ligation, a fluorescent ROS imaging sensor, which we validated for the specific experiment (Extended Data Fig. 3a–c), was enriched in the infarct, although to a lesser degree if neutrophils were depleted (Fig. 3a–c). We next interrogated available single-cell RNA sequencing (scRNA-seq) data for ROS-generating pathways in neutrophils²¹, comparing expression patterns to those of monocytes and macrophages isolated from mice with acute MI. Interestingly, the third most differentially regulated gene in neutrophils was *Lipocalin-2* (*Lcn2*) (Fig. 3d–f and Supplementary Table 1). Neutrophils rely on *Lcn2* to generate ROS while fighting bacteria²². However, this defense mechanism can become deleterious, damaging ischemic cardiomyocytes^{23,24}. Serum LCN2, also known as neutrophil gelatinase-associated lipocalin (NGAL), increases in patients with MI and heart failure and predicts infarct mortality and adverse outcomes²⁵. Motivated by these clinical data and by prior work linking ROS to arrhythmia²⁰, we hypothesized that neutrophils may trigger post-MI VT via *Lcn2*-related mechanisms.

Using quantitative RT-PCR in sorted immune cells, we verified that neutrophils express *Lcn2* at high levels when post-MI arrhythmias peak (Fig. 3g). Imaging in *Lcn2^{+/+}* and *Lcn2^{-/-}* mice revealed that *Lcn2* indeed promotes higher ROS flux rates in the acute infarct (Fig. 3h–j). To study the pro-arrhythmic relevance of neutrophil-derived *Lcn2*, we prepared *Lcn2^{+/+}* and *Lcn2^{-/-}* bone marrow

chimeras in which only bone-marrow-derived cells lack *Lcn2*. These mice then underwent the STORM procedure (Fig. 3k). Interestingly, we noticed that transplanting wild-type bone marrow into wild-type recipients produced a trend toward increased arrhythmias in STORM mice, implying that such cohorts are the appropriate controls (Extended Data Fig. 3d,e). In line with data obtained after neutrophil depletion, *Lcn2^{-/-}* bone marrow chimeras had a lower VT and Vfib burden than *Lcn2^{+/+}* bone marrow chimeras, even though overall neutrophil counts were unaffected in cardiac tissue (Fig. 3l,m and Extended Data Fig. 3f–k). These data support that neutrophils promote ventricular arrhythmia, at least partially, via *Lcn2*, which modulates ROS in the acutely ischemic myocardium.

Macrophages protect against ventricular arrhythmias. Given the profound effects that neutrophils have on post-MI arrhythmias, we suspected that macrophages may exert a similar influence. Coinciding with post-MI arrhythmias, cardiac macrophage numbers and phenotypes change markedly, as resident macrophage death and monocyte recruitment²⁶ begin shortly after ischemia onset. We tested how monocytes and macrophages influence post-MI arrhythmias with two different depletion strategies. First, we inhibited the colony-stimulating factor 1 receptor (Csf1R). This receptor promotes resident macrophage survival and myeloid cell proliferation²⁷. Ten days of Csf1R inhibition efficiently depleted cardiac macrophages even before MI, whereas serum potassium levels, left ventricular function and expression of cell death-associated genes remained unaffected (Extended Data Fig. 4a–f). The second depletion strategy relied on genetic deletion of the chemokine receptor *Ccr2*. *Ccr2^{-/-}* mice cannot mobilize monocytes from the bone marrow or recruit macrophages to the infarcted heart²⁸.

In mice without MI, rapid pacing induced similar VT in controls, in mice treated with Csf1R inhibitor (Extended Data Fig. 4g) or in *Ccr2^{-/-}* mice (Extended Data Fig. 4h). In hypokalemic mice without MI, macrophage depletion did not induce spontaneous VT or Vfib (Extended Data Fig. 4i,j). We next combined macrophage depletion with the STORM procedure. Csf1R inhibition depleted macrophages after MI (Fig. 4a,b), whereas neutrophil and monocyte counts, infarct size at 24 hours after coronary artery ligation and heart weight remained unaffected (Extended Data Fig. 5a–c). To our surprise, telemetric recordings in STORM mice treated with the Csf1R inhibitor revealed higher VT and Vfib burden compared to STORM controls (Fig. 4c,d and Extended Data Fig. 5d). We then deployed our second strategy—that is, inhibiting macrophage recruitment—in *Ccr2^{-/-}* STORM mice. This resulted in fewer infarct monocytes (Fig. 4e,f) presumably because, at early timepoints, these cells have not yet differentiated into macrophages. Neutrophils, infarct size and heart weight were similar to those in wild-type STORM controls (Extended Data Fig. 5e–g). *Ccr2^{-/-}* STORM mice had an increased post-MI VT and Vfib burden (Fig. 4g,h and Extended Data Fig. 5h). Macrophage depletion did not affect repolarization, as the QTc time remained unchanged (Extended Data Fig. 5i,j). In STORM mice, macrophage depletion did not alter survival in the first 24 hours after MI (Extended Data Fig. 5k). Altogether, these data suggest that macrophages play a protective role in MI-induced ventricular arrhythmias, irrespective of the cell subset. This insight motivated us to explore how macrophages exert such function in acute MI.

Macrophage depletion impairs efferocytosis in STORM mice. Given the opposite effects that we observed for neutrophils and macrophages, and that macrophages are thought to remove short-lived neutrophils from healing infarcts via phagocytosis²⁹, we first examined such interaction at the time when post-MI arrhythmia occurs. We employed flow cytometry in neutrophil reporter Ly6G^{TdTomato} mice³⁰ to test if macrophages phagocytose neutrophils 5 hours after coronary ligation. As expected, we clearly detected macrophages that

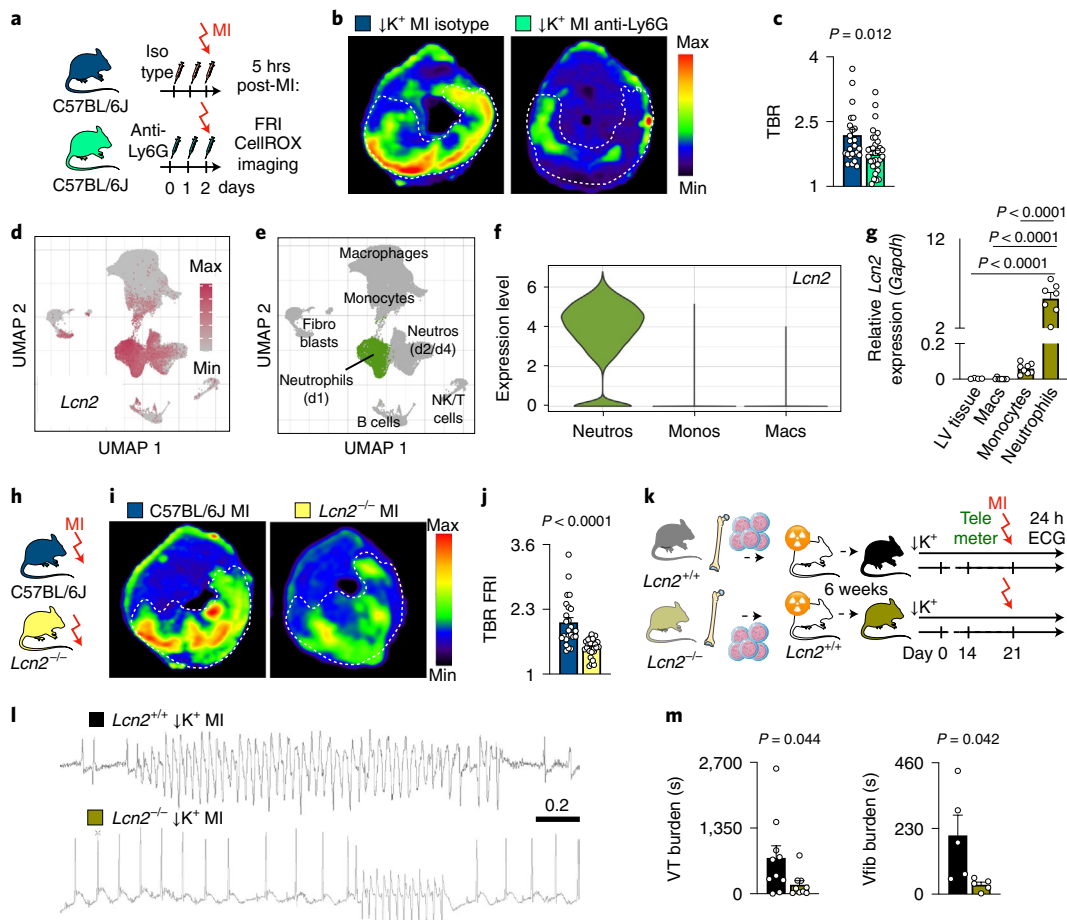


Fig. 3 | Neutrophil *Lcn2* promotes ventricular arrhythmia. **a**, Experimental outline. FRI of ROS in hearts 5 hours after MI using the CellROX imaging agent. **b**, Fluorescence images from cardiac short axis slices after injection of CellROX. **c**, Quantification of TBR from FRI. Data are from isotype antibody-injected controls ($n=6$ mice) and neutrophil-depleted mice ($n=7$). Each dot represents a cardiac slice. A two-sided Mann-Whitney test was used for statistical analysis. **d**, scRNA-seq data obtained in three mice after MI. Uniform manifold approximation and projection (UMAP) for dimension reduction indicates *Lcn2* expression and **(e)** cell population identities. **f**, Violin plots indicating *Lcn2* expression in neutrophils, monocytes and macrophages after MI ($n=3$ mice 24 hours after MI, $n=3$ mice 48 hours after MI and $n=8$ mice 4 days after MI; FDR < 0.001). **g**, *Lcn2* expression by quantitative PCR in ischemic myocardium ($n=4$ mice), flow-isolated macrophages (Macs) ($n=8$), monocytes (Monos) ($n=8$) and neutrophils (Neutros) ($n=7$) 5 hours after MI. *Lcn2* expression was normalized to *Gapdh*. A one-way ANOVA followed by Tukey's multiple comparisons test was used for statistical analysis. **h**, Experimental outline. FRI of ROS in *Lcn2*-deficient mice and *Lcn2*^{+/+} controls 5 hours after MI using CellROX sensor. **i**, Fluorescence images after intravenous CellROX injection. **j**, Quantification of TBR from FRI. Data are from *Lcn2*^{+/+} ($n=6$) and *Lcn2*^{-/-} ($n=4$) mice. Each dot represents a cardiac slice. A two-sided Mann-Whitney test was used for statistical analysis. **k**, Experimental outline. Bone marrow donors were either wild-type (*Lcn2*^{+/+}) or *Lcn2*^{-/-} mice. Transplant recipients were wild-type mice that subsequently underwent STORM protocol. **l**, ECG recordings from STORM *Lcn2*^{+/+} control and *Lcn2*^{-/-} bone marrow chimeras. **m**, VT burden and Vfib burden (*Lcn2*^{+/+} control, $n=8$ mice; *Lcn2*^{-/-}, $n=9$ mice) within 24 hours after MI. A two-sided Mann-Whitney test (VT burden) and two-sided unpaired t-test (Vfib burden) was used for statistical analysis. Data are mean \pm s.e.m. FDR, false discovery rate; LV, left ventricular; NK, natural killer.

had taken up neutrophils on day 3 after MI. However, macrophage-associated TdTomato fluorescence was extremely limited 5 hours after MI (Fig. 5a,b), when ventricular arrhythmias occurred. These data indicated that the anti-arrhythmic functions of macrophages cannot be explained by removal of pro-arrhythmic neutrophils.

Macrophages clear debris and apoptotic cells, a process termed efferocytosis, which is instrumental for tissue repair and infarct healing^{31,32}. Depleting macrophages may lead to accumulation of cellular debris and dead cells, which may give rise to heterogeneous conduction velocities or local conduction block, both considered key to re-entry and VT genesis. We, therefore, quantitated TUNEL⁺ cardiomyocytes in the infarcts of STORM controls, STORM mice with Csf1R inhibition and *Ccr2*^{-/-} STORM mice at the time of peak VT burden, 5 hours after permanent coronary ligation. As we had hypothesized, TUNEL⁺ cardiomyocytes accumulated more

readily in the infarcts of mice in which macrophages had been depleted (Fig. 5c-e).

Accelerated cell death may also cause higher accumulation of dead cells. Even though the final infarct size and survival measured 24 hours after ischemia was similar in STORM control and STORM macrophage depletion cohorts (Extended Data Fig. 5c,g,k), cardiomyocytes may die faster and at earlier timepoints when macrophages are absent, potentially contributing to the peak of arrhythmia prevalence at that time. Indeed, expression levels and activity of caspase-3, a mediator of programmed cell death, were higher in the infarct tissue of Csf1R inhibitor-treated and *Ccr2*^{-/-} STORM mice than in STORM controls (Fig. 5f,g). To evaluate cell death with an orthogonal method, we intravenously injected a near-infrared fluorescent Annexin-V molecular imaging probe, which binds to phosphatidyl serine on the surface of apoptotic cells and in the interior of

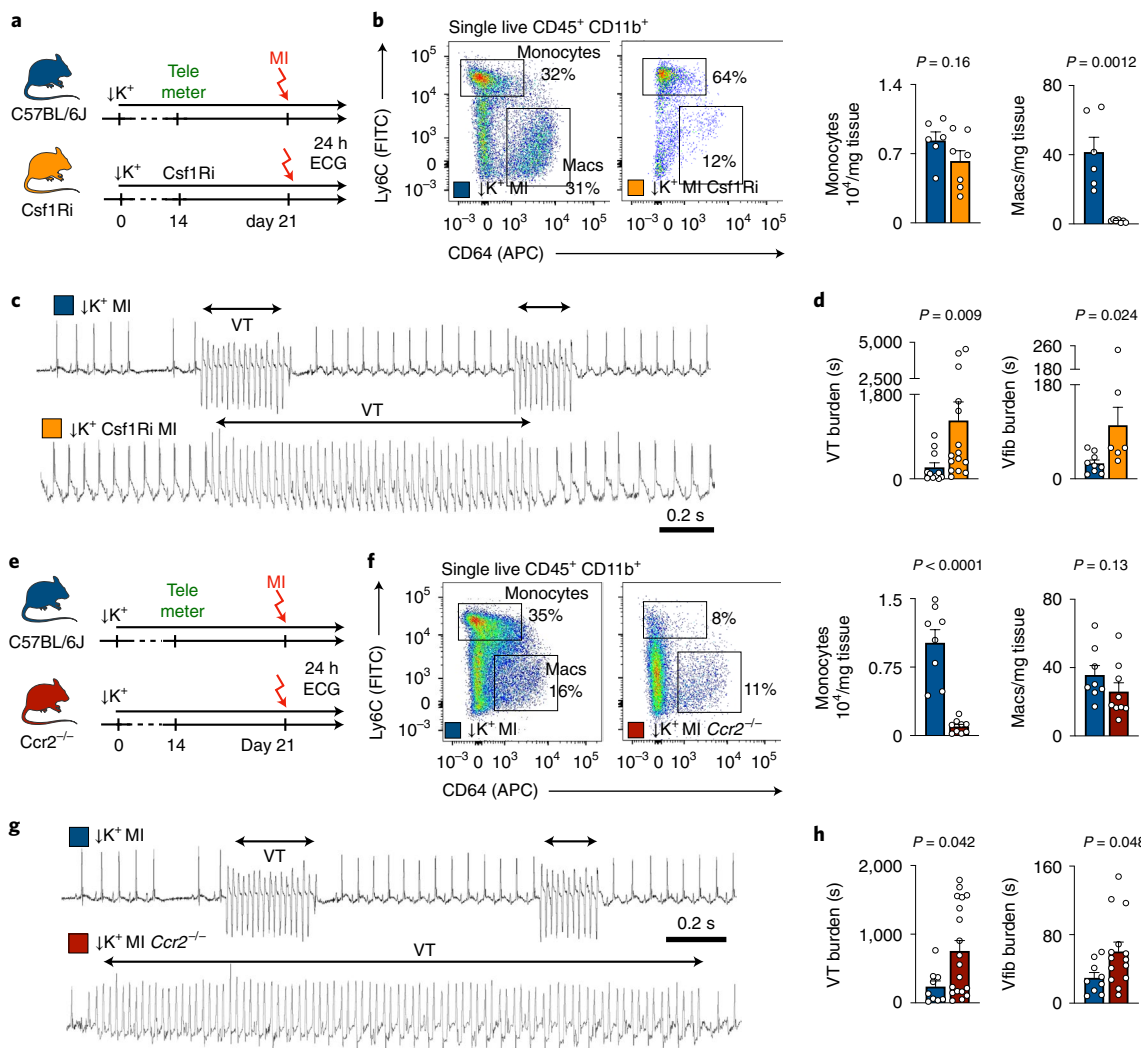


Fig. 4 | Macrophages protect against ventricular arrhythmia. **a**, Experimental outline for macrophage depletion with Csf1R inhibitor in STORM mice. **b**, Flow plots and quantification of cardiac monocytes and macrophages (Macs) in STORM control mice ($n=6$) and after macrophage depletion by Csf1Ri ($n=7$). A two-sided unpaired t-test (monocytes) and a two-sided Mann-Whitney test (macrophages) were used for statistical analysis. **c**, ECG recordings from STORM mice with and without macrophage depletion after MI. **d**, VT burden (STORM control mice, $n=11$; STORM Csf1Ri, $n=15$) and Vfib burden (STORM control mice, $n=6$; STORM Csf1R, $n=5$) within 24 hours after MI. Two-sided Mann-Whitney tests were used for statistical analysis. **e**, Experimental outline. **f**, Flow cytometry for cardiac monocytes and macrophages (Macs) in wild-type STORM control mice ($n=8$) and Ccr2^{-/-} STORM mice ($n=9$). A two-sided unpaired t-test (monocytes) and a two-sided Mann-Whitney test (macrophages) were used for statistical analysis. **g**, ECG recordings from wild-type STORM control and Ccr2^{-/-} STORM mice. **h**, VT burden (wild-type STORM control, $n=10$ mice; Ccr2^{-/-} STORM, $n=19$) and Vfib burden (wild-type STORM control, $n=8$; Ccr2^{-/-} STORM, $n=14$) after MI. Two-sided Mann-Whitney tests were used for statistical analysis. Data are mean \pm s.e.m.

necrotic cells³³, 4 hours after MI and harvested the hearts 60 minutes later. In all three cohorts, fluorescent reflectance imaging (FRI) of cardiac short axis slices showed binding of the imaging probe primarily in the infarcts. We also found higher target-to-background ratios (TBRs) in the infarcts of Csf1R inhibitor-treated and Ccr2^{-/-} STORM mice when compared to STORM controls (Fig. 5h,i). From these data, we concluded that, in the absence of macrophages, cardiomyocytes may die at higher rates 5 hours after onset of ischemia. Disrupted removal of dead cells may also contribute to their accumulation.

Macrophage depletion compromises mitochondrial function after MI. The accelerated cardiomyocyte demise in mice without macrophages raised the question of how macrophages defend myocytes against ischemic cell death. The primary cause of hypoxic

cell death is energy deficit due to disrupted mitochondrial function, and these organelles also induce programmed cell death when under duress³⁴. Interestingly, stressed cells may shed mitochondria in relatively large extracellular vesicles¹⁰. Cardiac macrophages may augment mitochondrial function in cardiomyocytes by scavenging dysfunctional organelles expelled in vesicles called exophers, supporting steady-state cardiomyocyte metabolism and overall organ function¹⁰. Furthermore, dysfunctional mitochondria give rise to arrhythmia via ROS and ATP deprivation as ~30% of cardiomyocytes' energy consumption supports ion handling needed for proper excitation⁴.

To explore how macrophage depletion affects mitochondrial health in acute MI, we first performed transmission electron microscopy (TEM) in infarct tissue obtained from STORM mice with and without macrophage depletion, 5 hours after coronary

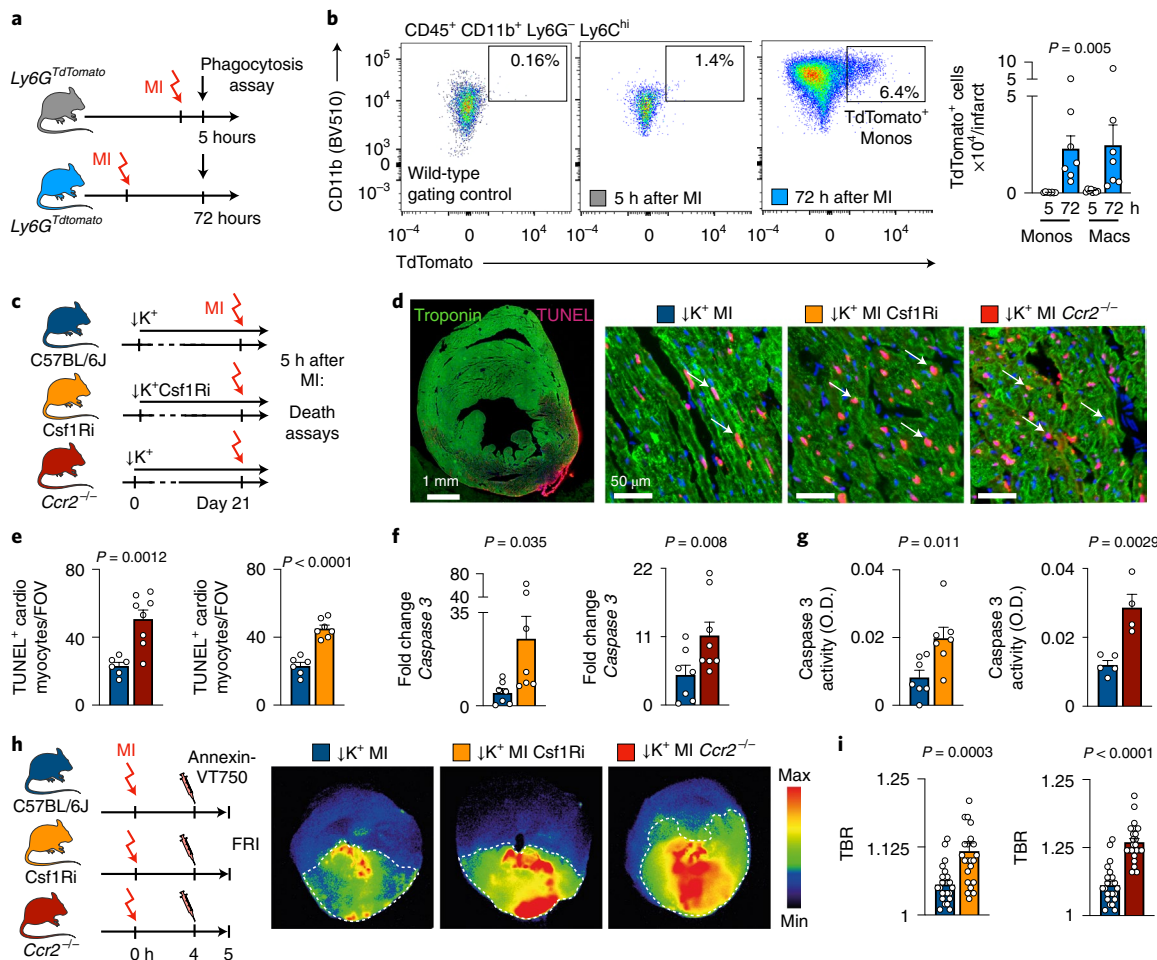


Fig. 5 | Macrophage depletion accelerates myocyte death and impairs efferocytosis during acute MI. **a**, Experimental outline. **b**, Flow plots after gating for cardiac macrophages (Macs). Bar graphs show quantification of TdTomato⁺ cardiac monocytes (Monos) and TdTomato⁺Macs at 5 hours ($n=7$ mice) or 72 hours ($n=7$ mice) after MI. One-way ANOVA followed by Tukey's multiple comparison's test was used for statistical analysis. **c**, Experimental outline for wild-type C57BL/6 mice, mice after Csf1Ri macrophage depletion and *Ccr2^{-/-}* mice, all after STORM protocol. **d**, TUNEL, troponin and DAPI staining of sections from the infarct region 5 hours after MI. Scale bar, 50 μ m. This experiment was repeated independently twice. **e**, Analysis of TUNEL⁺ myocytes in hearts of C57BL/6 mice ($n=6$), mice treated with Csf1Ri ($n=7$) and *Ccr2^{-/-}* mice ($n=8$), all after STORM protocol. FOVs were analyzed in the infarct core. Two-sided unpaired *t*-tests were used for statistical analysis. **f**, Caspase-3 expression by quantitative PCR in infarct tissue from C57BL/6 mice ($n=7$), mice treated with Csf1Ri ($n=7$) and *Ccr2^{-/-}* mice ($n=8$), all after STORM protocol. Data from macrophage depletion groups were normalized to data from STORM mice. Two-sided Mann-Whitney tests were used for statistical analysis. **g**, Enzymatic activity of Caspase-3 measured in left ventricular infarct tissue from C57BL/6 mice ($n=5$ (left) or $n=7$ (right)), mice treated with Csf1Ri ($n=7$) and *Ccr2^{-/-}* mice ($n=5$). Two-sided unpaired *t*-tests were used for statistical analysis. **h**, Experimental outline and images from FRI after intravenous injection of Annexin-VT750. **i**, TBR from FRI. Data are from $n=4$ -5 mice per group. Each dot represents a cardiac slice from an infarcted mouse. Two-sided Mann-Whitney tests were used for statistical analysis. Data are mean \pm s.e.m.

ligation. MI led to mitochondrial swelling and ultrastructure loss, as indicated by reduced cristae (Extended Data Fig. 6a,b). When macrophages were depleted, the number of dysmorphic mitochondria increased in cardiomyocytes (Fig. 6a–c). In mice with macrophage depletion, cardiomyocytes' mitochondria were smaller, and the area covered by cristae was smaller than in STORM controls, indicating accelerated structural and functional mitochondrial collapse³⁵, presumably after rupture (Fig. 6d,e). Paracrystalline inclusions, a hallmark of cellular energy deprivation³⁶, were more frequent in mitochondria of macrophage depletion groups (Fig. 6f,g and Extended Data Fig. 6c,d). We next focused on extracellular mitochondria. We observed such mitochondria in two different forms, either freely positioned in the extracellular space (Fig. 6h) or inside vesicles (Extended Data Fig. 6e) that resembled previously described exopher-like structures¹⁰. In addition, mitochondria were also located adjacent to and inside phagocytic cells

(Extended Data Fig. 6f,g). These data suggest that macrophages clear cardiomyocyte-derived mitochondria in STORM mice at 5 hours after MI. In Csf1R inhibitor-treated and *Ccr2^{-/-}* STORM mice, free extracellular mitochondria were more numerous (Fig. 6i), indicating that mitochondrial removal was impaired when macrophages were absent. Of note, some mitochondrial deterioration after macrophage depletion was observed in mice without MI (Extended Data Fig. 6h–k), indicating that mitochondrial compromise preceded ischemia.

On a functional level, macrophage depletion lowered activity of the mitochondrial respiratory chain enzymes succinate dehydrogenase (complex II) and cytochrome c oxidase (complex IV) (Fig. 6j,k). Enzymes of the mitochondrial respiratory chain pump protons across the inner mitochondrial membrane, producing a transmembrane electrical potential gradient ($\Delta\Psi_m$) that is essential for ATP synthesis³⁷. In conditions of cell death and compromised

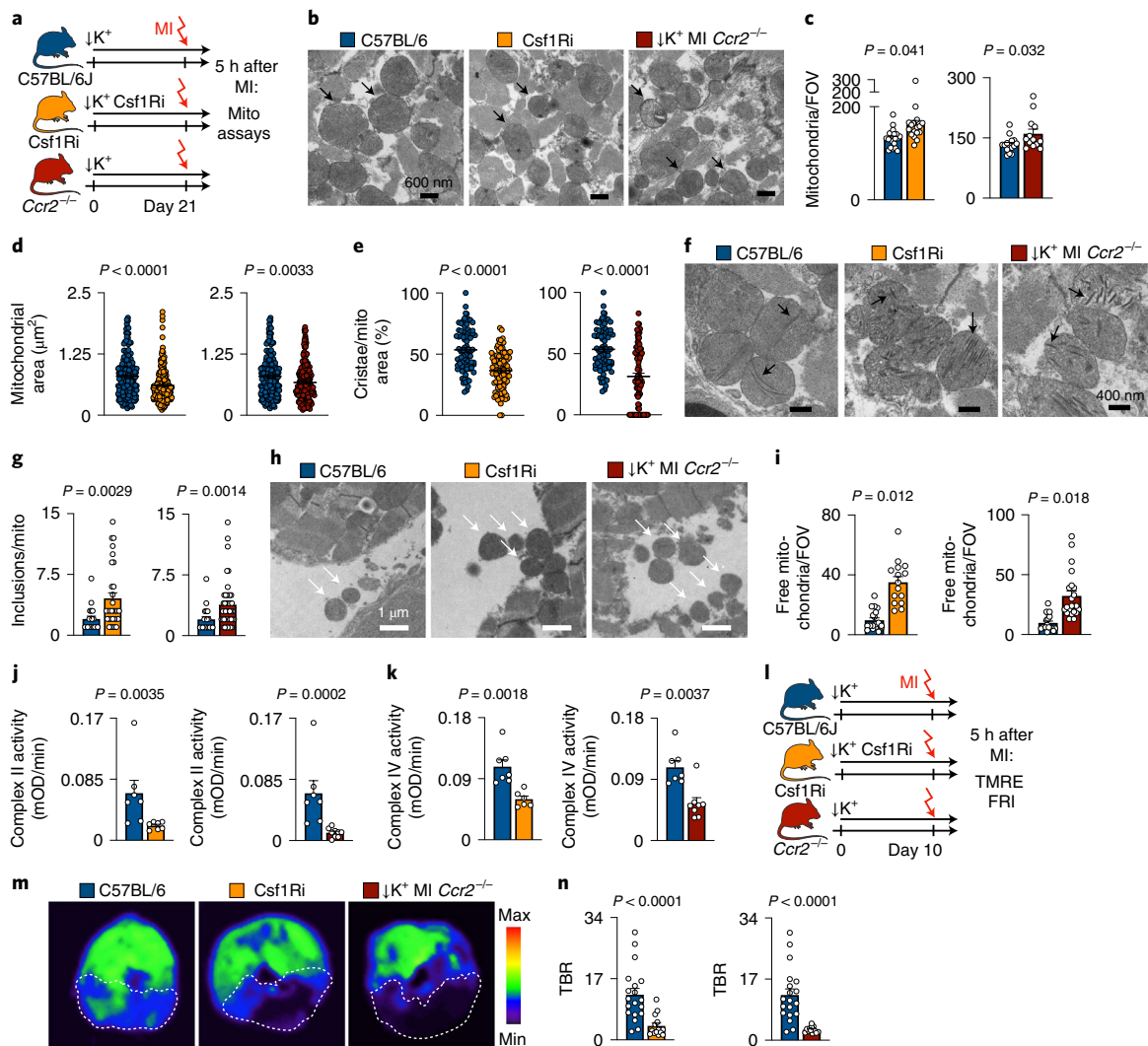


Fig. 6 | Macrophages preserve mitochondrial integrity after MI. **a**, Experimental outline. **b**, Electron microscopy in infarcts. Arrows indicate mitochondria; scale bar, 600 nm. This experiment was repeated independently three times. **c**, Mitochondrial count per FOV in wild-type mice ($n=15$ FOVs), mice with Csf1Ri ($n=21$) and Ccr2^{-/-} mice ($n=13$) ($n=3$ mice per group, 3–5 FOVs per mouse). A two-sided nested t-test was used. **d**, Mitochondrial area in infarcts of wild-type mice ($n=178$ mitochondria), mice after Csf1Ri ($n=239$) and Ccr2^{-/-} mice ($n=229$) ($n=3$ mice per group; 5 FOVs per mouse). Dots indicate individual mitochondria. A two-sided Mann–Whitney test was used. **e**, Percent cristae area per mitochondrial area in infarcts of wild-type ($n=80$ mitochondria), mice with Csf1Ri ($n=98$) and Ccr2^{-/-} mice ($n=87$) ($n=3$ mice per group, 10 FOVs per mouse). Each dot represents a mitochondrion. A two-sided unpaired t-test (Csf1Ri) and Mann–Whitney test (Ccr2^{-/-}) was used. **f**, Electron micrographs of mitochondrial ultrastructure with paracrystalline inclusions (arrows). **g**, Paracrystalline inclusions per mitochondrion in wild-type ($n=19$ mitochondria), after Csf1Ri macrophage depletion ($n=31$) and Ccr2^{-/-} mice ($n=44$). Dots are mitochondria. A two-sided Mann–Whitney test was used. **h**, Electron micrographs of free mitochondria (arrows) in the extracellular space. Scale bar, 1 μm . This experiment was repeated independently three times. **i**, Free mitochondria in wild-type ($n=15$ FOVs), mice with Csf1Ri ($n=15$) and Ccr2^{-/-} mice ($n=19$) ($n=3$ mice per group, 5–7 FOVs per mouse). A two-sided nested t-test was used. **j**, Enzymatic activity of mitochondrial complex II in infarcts of wild-type ($n=7$ mice), after Csf1Ri ($n=7$) and Ccr2^{-/-} mice ($n=9$). A two-sided Mann–Whitney test was used. **k**, Enzymatic activity of mitochondrial complex IV in infarcts of wild-type ($n=7$ mice), after Csf1Ri ($n=6$) and Ccr2^{-/-} ($n=8$), all after STORM protocol. A two-sided Mann–Whitney test was used. **l**, Experimental outline of TMRE perchlorate imaging. **m**, Representative images of TMRE imaging. **n**, TBR from FRI. STORM mice ($n=19$ slices), STORM mice with Csf1Ri ($n=14$) and STORM Ccr2^{-/-} mice ($n=12$). Data are from $n=3$ or $n=4$ mice per group. Dots indicate cardiac slices. A two-sided Mann–Whitney test was used. Data are mean \pm s.e.m.

mitochondrial integrity, the $\Delta\Psi_m$ diminishes³⁸. To test for loss of mitochondrial $\Delta\Psi_m$ in macrophage depletion cohorts, we intravenously injected tetramethylrhodamine ethyl ester (TMRE), a positively charged lipophilic fluorescent imaging agent that accumulates inside negatively charged mitochondria. Fifteen minutes after TMRE injection, we imaged myocardial short axis slices ex vivo. In a pilot imaging experiment, treatment with a mitochondrial uncoupler, which reduces $\Delta\Psi^39$, changed the myocardial TMRE accumulation accordingly, thereby validating this imaging assay (Extended

Data Fig. 6l,m). Macrophage depletion with Csf1R inhibition and in Ccr2^{-/-} mice resulted in decreased myocardial fluorescence signal in non-infarcted hearts (Extended Data Fig. 6n,o) and also in the infarcted myocardium (Fig. 6l–n), suggesting that macrophages may preserve cardiomyocytes' mitochondrial $\Delta\Psi_m$. These imaging data accord with reduced activity of mitochondrial complex II and IV observed after macrophage depletion, collectively supporting the concept of impaired mitochondrial integrity and function in macrophage-depleted myocardium.

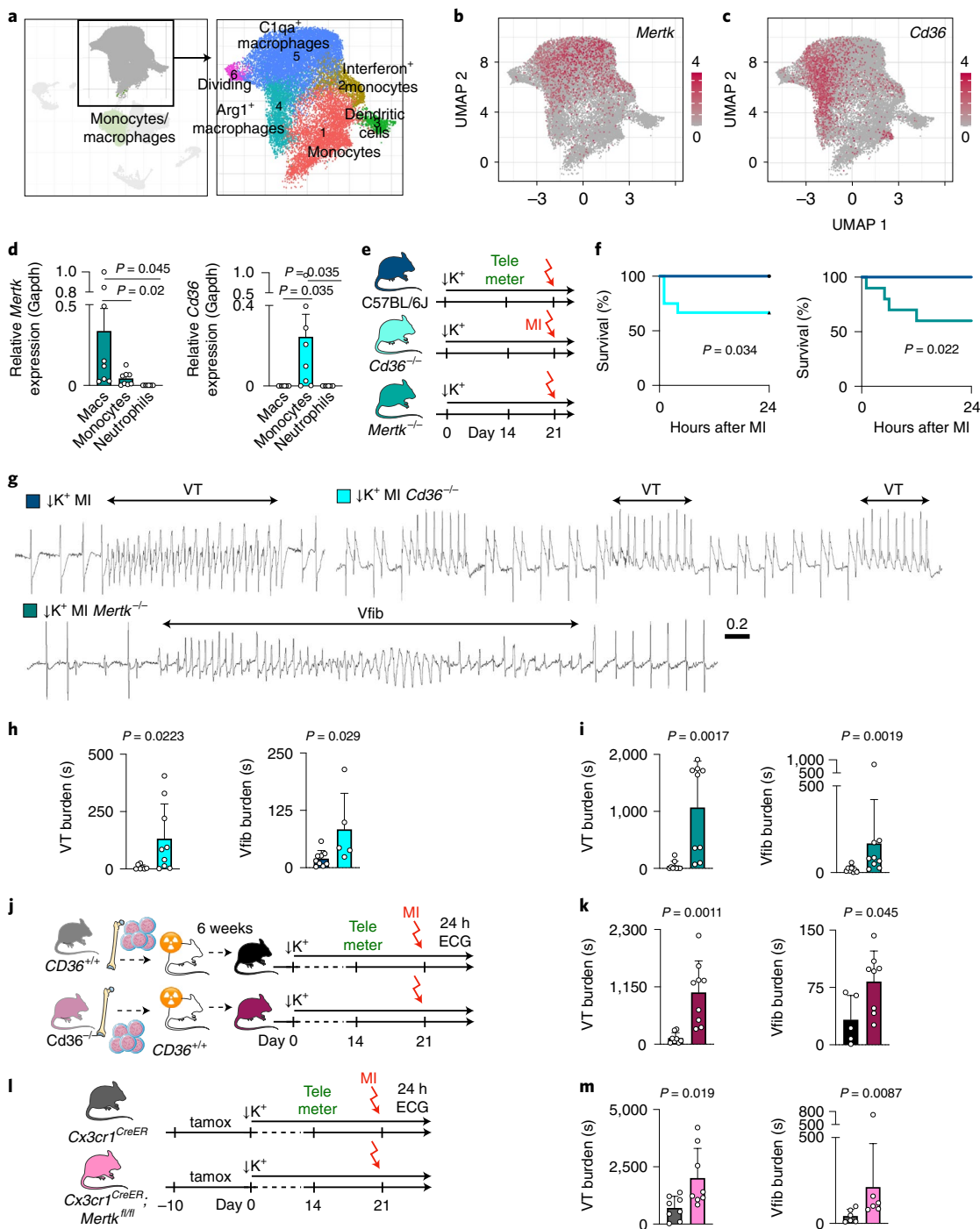


Fig. 7 | Phagocytosis receptor deletion causes sudden cardiac death. **a**, scRNA-seq data from $n=3$ mice each on days 1, 2 and 4 after MI. Uniform manifold approximation and projection (UMAP) indicates cell subset. **b**, UMAP of Mertk expression by cell populations shown in **a**. **c**, UMAP of Cd36 expression by cell populations shown in **a**. **d**, Mertk and Cd36 expression in flow-sorted macrophages (Macs) ($n=8$ mice), monocytes ($n=8$ mice) and neutrophils ($n=7$ mice) 5 hours after MI, normalized to Gapdh. One-way ANOVA followed by Tukey's multiple comparisons test were used for statistical analysis. **e**, Experimental outline. C57BL/6, Cd36^{-/-} and Mertk^{-/-} mice underwent STORM protocol. **f**, Kaplan-Meier survival curve of wild-type ($n=14$ mice, left, and $n=11$ mice, right), Cd36^{-/-} ($n=14$) and Mertk^{-/-} ($n=10$) mice. P values were calculated using the log-rank (Mantel-Cox) test. **g**, ECG recordings from C57BL/6, Cd36^{-/-} and Mertk^{-/-} mice, all after STORM procedure. **h**, VT burden and Vfib burden in C57BL/6 mice ($n=9$) and Cd36^{-/-} mice ($n=9$) after STORM procedure, within 6 hours after MI. A two-sided Mann-Whitney test was used for statistical analysis. **i**, VT burden and Vfib burden in C57BL/6 mice ($n=8$) and Mertk^{-/-} mice ($n=9$) after STORM procedure, within 6 hours after MI. Two-sided Mann-Whitney tests were used for statistical analysis. **j**, Experimental outline. Bone marrow donors were either wild-type or Cd36^{-/-} mice. Recipient wild-type mice underwent STORM protocol. **k**, VT burden and Vfib burden in wild-type controls (Cd36^{+/+}, $n=8$ mice) or Cd36^{-/-} ($n=9$) bone marrow chimeras 24 hours after MI. Two-sided Mann-Whitney tests were used for statistical analysis. **l**, Experimental outline. Cx3cr1^{CreER2}; Mertk^{fl/fl} mice and Cx3cr1^{CreER2} control mice were fed a tamoxifen (tamox) diet for 10 days. All mice underwent STORM protocol after tamoxifen exposure. **m**, VT burden and Vfib burden in Cx3cr1^{CreER2} controls ($n=8$ mice) or Cx3cr1^{CreER2}; Mertk^{fl/fl} mice ($n=8$) 24 hours after MI. A two-sided unpaired *t*-test (VT burden) and a Mann-Whitney test (Vfib burden) were used for statistical analysis. Data are mean \pm s.e.m.

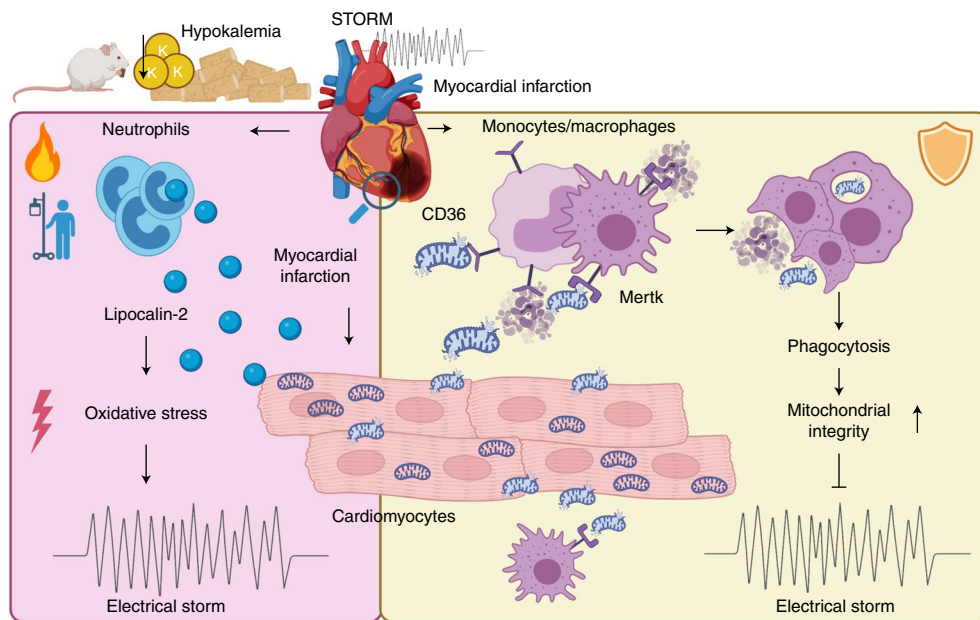


Fig. 8 | Summary of findings.

Phagocytosis receptor function prevents sudden cardiac death.

Macrophage scavenger receptors recognize phosphatidylserine on apoptotic cells, thus enabling efferocytosis⁴⁰. Cluster of differentiation (Cd) 36 facilitates apoptotic and necrotic cardiomyocyte uptake, particularly during the early hours after MI⁴¹. Cd36-enabled efferocytosis permits cardiac repair after ischemia³². The MER receptor tyrosine kinase (Mertk) similarly mediates efferocytosis and, in addition, facilitates the removal of dysfunctional mitochondria from cardiomyocytes¹⁰. To test the role of these receptors in MI-related ventricular arrhythmia, we first examined their expression by monocytes and macrophages after MI. In available scRNA-seq data obtained on days 1–4 after MI²¹ (Fig. 7a–c), followed up with quantitative RT–PCR in cells flow sorted 5 hours after MI (Fig. 7d), we found *Mertk* predominantly expressed by macrophages. *Cd36* was highly expressed by recruited monocytes at 5 hours after MI, but it was more broadly expressed by macrophages in the scRNA-seq data that were acquired at later timepoints when monocytes may have differentiated (Fig. 7c,d). Neither gene was expressed by neutrophils (Fig. 7d). We then exposed *Cd36*^{−/−} and *Mertk*^{−/−} mice to the STORM procedure. Unlike wild-type STORM controls, *Cd36*^{−/−} and *Mertk*^{−/−} STORM mice developed sudden cardiac death, as long VT episodes deteriorated into Vfib (Fig. 7e–g and Extended Data Fig. 7a,b). Of note, we did not observe myocardial rupture, which typically happens several days after an infarct and, therefore, likely did not contribute to the high mortality recorded here. Both *Cd36*^{−/−} and *Mertk*^{−/−} mice had increased VT and Vfib burden (Fig. 7h,i). Interestingly, *Mertk*^{−/−} STORM mice, but not *Cd36*^{−/−} STORM mice, had a higher Vfib incidence than STORM controls (Extended Data Fig. 7c,d), perhaps due to differences in cell subset expression of phagocytosis receptors. We next used chimeras, in which only bone-marrow-derived leukocytes lacked *Cd36* expression, to specifically exclude contributions of *Cd36* expressed by cardiomyocytes. Wild-type controls were also lethally irradiated but received *Cd36*^{+/+} bone marrow. When these cohorts underwent the STORM protocol, *Cd36*^{−/−} chimeras had elevated VT and Vfib burden, confirming the key leukocyte contribution to the anti-arrhythmic function of *Cd36* (Fig. 7j,k and Extended Data Fig. 7e,f). Finally, we bred *Cx3cr1*^{CreERT2} mice, which efficiently target macrophages upon tamoxifen exposure (Extended Data Fig. 7g), with *Mertk*^{−/−} mice,

resulting in macrophage-specific *Mertk* deletion. When exposed to the STORM procedure, *Cx3cr1*^{CreERT2}, *Mertk*^{−/−} mice presented with increased VT and Vfib burden (Fig. 7l,m and Extended Data Fig. 7h,i), similarly to mice with global *Mertk* deletion. These data confirm that macrophage expression of *Mertk* protects against post-MI ventricular arrhythmias.

Discussion

Myocytes and the specialized conduction system cells are responsible for cardiac excitation, and these cells' dysfunction is the primary cause of arrhythmias. It has been known for decades that stromal cells may affect the cardiac rhythm by interacting with conducting cells. For instance, fibroblasts influence conduction indirectly via matrix deposition and directly via electrotonic coupling⁴². That macrophages participate in conduction is a more recent insight⁹, as even the existence of resident cardiac macrophages has emerged only recently^{8,43}. Even though it remains unsettled how exactly leukocytes participate in arrhythmogenesis⁴⁴, it is generally accepted that inflammation propagates rhythm disorders⁴⁵. This notion rests on the clinical association of arrhythmia with inflammatory disorders—for example, myocarditis or sepsis—and with blood biomarkers, such as C-reactive protein or IL-6 (ref. ⁴⁴). Furthermore, genetically enforced inflammasome activation in cardiomyocytes leads to inducible atrial arrhythmia in mice⁴⁶. In the current work, we have identified how the most abundant cardiac leukocyte populations, specifically neutrophils and macrophages, influence ischemia-induced ventricular arrhythmias (Fig. 8).

Neutrophil depletion reduced VT burden, identifying these cells as proponents of ventricular arrhythmia in mice with an acute MI. A key neutrophil defense protein, Lcn2, increases ROS in cardiomyocytes²⁴. Lcn2 could, thus, modulate ion channel proteins and their function by oxidation, which might change action potential duration and calcium handling. These alterations induce heterogeneity in conduction velocity, delayed afterdepolarizations and re-entry that underlie VT and Vfib²⁰. We found that, similarly to neutrophil depletion, deleting Lcn2 from bone-marrow-derived leukocytes reduced the arrhythmia burden. These data align well with the observation that the prototypical neutrophil enzyme myeloperoxidase promotes atrial fibrillation via oxidative protein modifications⁴⁷.

In contrast to neutrophils, macrophages protect against post-MI arrhythmias. Either inhibiting the Csf1 receptor, which reduces all macrophages irrespective of their source, or genetically deleting the chemokine receptor Ccr2, which abrogates recruitment of a macrophage subset considered inflammatory⁴⁸, increased VT burden. A primary function of macrophages early after MI is phagocytosis of dead cardiomyocytes, a process that promotes wound healing after ischemia¹¹. Removal of dead cells by monocytes and macrophages relies on Cd36 and Mertk receptors^{31,32,41}. Genetic deletion of these receptors led to lethal arrhythmias in mice with acute MI. Impaired removal of dead or damaged cells may slow regional conduction and increase electrical heterogeneity in the myocardium, both of which are potential substrates for re-entry and ventricular arrhythmias^{6,49}. In addition, our data suggest that macrophages may decelerate myocyte death during ischemia. Although infarct size 24 hours after permanent coronary ligation, which is governed by the site of the coronary artery ligation, was similar in mice with and without macrophages, TUNEL and caspase assays obtained 5 hours after MI, when VT and Vfib were most common, indicated that myocytes perished more slowly if macrophages were present. Because cardiac resident macrophages preserve myocytes' metabolic health through scavenging dysfunctional mitochondria¹⁰, it is conceivable that the lack of macrophages, which preceded ischemia in our experiments, hastened mitochondrial failure. Indeed, depleting macrophages accelerated mitochondrial membrane potential collapse in ischemic myocytes. This, in turn, may have drained ATP faster, possibly jeopardizing ion pump function and Ca handling⁵⁰. Additional mechanisms influencing cardiomyocyte autophagy⁵¹ might contribute to the accumulation of dysfunctional mitochondria in the absence of macrophages. Ultimately, mitochondrial failure induces cell death³⁴, a catastrophic event that produces complete loss of regional conduction. The resulting local block may add to the myocardium's electrical heterogeneity.

The observed protective macrophage functions after ischemia accord with their supportive roles in AV node conduction^{9,52}. These cells facilitate conduction via gap junction coupling⁹ or, in the setting of pulmonary hypertension, by secreting amphiregulin, which preserves gap junction communication between myocytes⁵². Macrophage death during ischemia may deprive the ischemic myocardium of such support. We suspect that there are likely additional aspects to macrophages' beneficial roles, such as modulating sympathetic cardiac innervation⁵³, cytokine signaling or scavenging tissue microenvironment, which may, in turn, influence the ability of myocytes to survive or conduct.

We began investigating the causal roles of leukocytes in ventricular arrhythmia by studying mice with no comorbidities beyond ischemia and hypokalemia. Although this is a reasonable starting point, it differs from the clinical scenario, which includes comorbidities and cardiovascular risk factors. Such comorbidities may raise systemic leukocyte numbers and skew the cell repertoire toward inflammatory phenotypes⁵⁴. We found that depleting macrophages or their receptors promoted post-MI electrical storm; however, macrophage oversupply may also be pro-arrhythmic. In *apoE*^{-/-} mice with pre-existing atherosclerosis, rapid pacing more efficiently induces ventricular arrhythmia on day 5 after ischemia⁵⁵. In mice and patients, atherosclerosis increases leukocyte production, which, in turn, elevates infarct inflammation²⁶. Thus, future studies should evaluate how macrophage oversupply, or inflammatory phenotypic bias, influences arrhythmia. Our clinical data on the pro-arrhythmic effects of neutrophils support such a hypothesis. The contribution of cardiac leukocytes to arrhythmia likely varies according to the underlying substrate, presumably with a lower contribution to VT arising from chronic scarring and greatest relevance for conditions with acute inflammatory myocardial injury, including infarction as tested here and, potentially, also myocarditis, cardiomyopathies or sarcoidosis.

These follow-up questions—for example, regarding the roles of leukocytes during reperfusion or how to identify harmful macrophage and lymphocyte subsets—can be addressed with the straightforward STORM mouse model of spontaneous VT and Vfib. Because STORM does not rely on genetic manipulation of cardiomyocytes, it enables leukocyte-specific and fibroblast-specific genetic loss-of-function studies. The STORM model also has limitations, most of which it shares with any arrhythmia studies in mice. Compared to humans and large animals, mice have a higher heart rate, a shorter and differently shaped action potential, diverging ion channel functions and a smaller ventricle that may affect re-entry¹². A specific limitation of the STORM model pertains to its reliance on hypokalemia, as only a subset of patients is hypokalemic. It is, therefore, important to examine leukocyte actions on ventricular arrhythmia in more suitable large animals, such as normokalemic pigs or dogs⁵⁶. Ultimately, only prospective clinical trials will illuminate whether leukocyte-targeted interventions reduce arrhythmia in humans.

This work was directed by clinical questions and shows that neutrophil depletion could be a therapeutic opportunity to curb ischemia-triggered electrical storm. However, beneficial properties of neutrophil subsets after MI⁵⁷ indicate that broad cell depletion may be problematic. Co-existing beneficial and detrimental cell functions are a common phenomenon for immune cells⁵⁸. For example, in the setting of bacterial meningitis, neutrophils defend against infection by removing bacteria but also inflict permanent nerve damage that can lead to deafness in the survivors^{59,60}. Neutralizing specific pro-arrhythmic neutrophil products, perhaps even lipocalin-2, may limit negative side effects on infarct healing and immune defense. To our surprise, all macrophage subsets, including monocyte-derived macrophages that often fuel detrimental inflammation, appear to protect against post-MI arrhythmia, raising the possibility that overzealous macrophage targeting enables arrhythmia. Csf1R and CCR2 inhibition, or other immunotherapeutics that interfere with the heart's leukocyte reservoir, may compromise cardiac mitochondrial health, myocyte metabolism and conduction. Taken together, our results demonstrate that leukocytes are causally implicated in ischemia-induced VT, which motivates studying participation of this cell class in electrophysiological pathologies beyond MI, especially in conditions with inflammatory components. Understanding specific arrhythmia-promoting immune cell functions may enable developing a new class of immunomodulatory anti-arrhythmic drugs.

Methods

Human subjects. Patients with MI (STEMI) who underwent PPCI at Oxford University Hospitals were enrolled into the Oxford Acute Myocardial Infarction study between 2010 and 2020 (ref. ⁶¹), which complies with the Declaration of Helsinki and was approved by a local research ethics committee (10/H0408/24). Patients were excluded if they had a late presentation with symptom duration >12 hours, cardiogenic shock, previous coronary artery bypass grafting, severe heart valve disease, contraindication to MRI, age >85 years, diagnosis of sepsis or infection during the same episode or use of immunosuppressants. Verbal assent at the time of PPCI was followed by informed written consent. No financial compensation was offered for participation, although study-related travel expenses could be reimbursed. After PPCI, patients underwent continuous ECG monitoring for at least 24 hours⁶². These records were used to establish a prospectively defined arrhythmia score for each patient: (i) no arrhythmia, (ii) ventricular ectopic beats, (iii) non-sustained VT and (iv) sustained VT (>30 seconds or requiring cardioversion) or Vfib. Patients underwent MRI at a median of 2 days after PPCI^{61,63}. Statistical analyses for the Oxford cohort were performed using GraphPad Prism 9 (GraphPad Software), IBM SPSS for Macintosh version 28.0.0.0 (version 27.0, IBM) and RStudio version 1.4.1717. MRI analyses were conducted using cvi42 (Circle Cardiovascular Imaging). Statistical testing for the presence of a trend across arrhythmia score groups according to the neutrophil count was performed using the Jonckheere–Terpstra test⁶⁴ as implemented in the clinfun package⁶⁵ in R version 4.1.1. Clinical risk factors for arrhythmias include cardiogenic shock, late presentation after onset of symptoms and larger infarct size while prior beta-blocker usage is protective^{62,66}. Patients with cardiogenic shock or presentation >12 hours from onset of symptoms were excluded. To adjust for ischemic time, beta-blockers and the MI size measured using MRI, logistic

regression analysis was performed. The first level of the binary outcome was the composite of no arrhythmia or ventricular ectopic beats, and the second level of the binary outcome was the composite of non-sustained VT, sustained VT or Vfib. The logistic regression model was statistically significant ($P < 0.001$), correctly classifying 68% of cases. Neutrophil count ($P < 0.001$) and acute MI size ($P = 0.004$) contributed significantly to the model, whereas the use of beta-blockers ($P = 0.53$) and ischemic time ($P = 0.57$) did not. Neutrophil count continued to contribute significantly to the adjusted model (each 1×10^9 per L increase in neutrophil count was associated with a 20% relative increase in the risk of ventricular arrhythmia ($HR = 1.20$, 95% CI: 1.056–1.36, $P = 0.003$)) as did MI size (for each 1% increase in acute MI size, $HR = 1.02$, 95% CI: 1.000–1.048, $P = 0.048$).

To investigate links between neutrophil counts and MI outcomes, human subject data were collected retrospectively at Mass General Brigham. The research was approved by the Partners Healthcare Institutional Review Board, and the need for individual informed consent was waived. No financial compensation was offered. The Partners Data Warehouse is linked to the Social Security Death Index, assuring a high degree of completeness of follow-up. We collected data from hematological testing and clinical MI outcomes between June 2015 and June 2020. Inclusion criteria included (1) diagnosis of NSTEMI or STEMI, (2) increased troponin, (3) white cell differential within 24 hours before or 48 hours after the first positive troponin and (4) age 40–85 years. Patients were excluded if they had sepsis or infection during MI. For patients with multiple neutrophil counts, the maximum value was used. Analyses for the Mass General Brigham cohort were performed using GraphPad Prism 9, IBM SPSS for Macintosh version 28.0.0.0 (version 27.0) and RStudio version 1.4.1717, implementing the survival package (version 3.2-13) downloaded from <https://CRAN.R-project.org/package=survival>. The pre-specified clinical outcomes of interest were a composite of cardiac arrest or all-cause death at 30 days. The cohort was dichotomized at the median neutrophil count of 6.6×10^9 per L. We used the proportional hazard test⁴⁷ as implemented by the cox.zph command in the Survival package⁴⁸ in R version 4.1.1 to test the proportional hazards assumption against non-proportional hazards (that is, time-varying coefficients). For time-to-event analysis, the start date was defined as the date of the positive troponin test triggering a diagnosis of MI. To adjust for covariates, a series of Cox regression models adjusted for the effects of age; sex; peak troponin level; STEMI diagnosis; other components of the white cell count differential, including peak monocyte count and peak basophil count; and peak creatinine were constructed.

Mice. Experiments were approved by the Massachusetts General Hospital Institutional Animal Care and Use Committee, performed in compliance with relevant ethical regulations, and all efforts were made to avoid suffering of animals. Wild-type C57BL/6J, tamoxifen-inducible *B6J.B6N(Cg)-Cx3cr1tm1.1cre*^{Jung/J} (*Cx3cr1*^{CreERT2}), *B6.SJL-Ptprc^a Pep^b/BoyJ* (*Cd45.1*), *B6.129S4-Ccr2tm1Ifc/J* (*Ccr2*^{-/-}), *B6.129P2-Lcn2tm1Aade/AkiJ* (*Lcn2*^{-/-}), *B6.129S1-Cd36tm1Mf/J* (*Cd36*^{-/-}), *B6.129-Mertk^{tm1}Grl/J* (*Mertk*^{-/-}), *B6.129(Cg)-Gt(ROSA)26Sor^{tm4(ACTB-tdTOMato-EGFP)}Luo/J*, *B6.FVB-Tg(Myh6-cre)2182Mds/J* and *B6.Cg-Gt(ROSA)26Sor^{tm9(CAG-tdTOMato)Hze/J}* (*Ai9*) mice were purchased from The Jackson Laboratory. *Mertk*^{tm1} mice were provided by Carla Rothlin (Yale University)⁴⁹. *B6.Cg-Tg(Myh6-GCaMP8)B4-10Mik/J* (*Myh6-GCaMP8*) mice were provided by Cornell Heart Lung Blood Resource for Optogenetic Mouse Signaling. *Ly6G-Cre* mice were provided by Mikael Pittet (Massachusetts General Hospital); breeders received from the Institute for Experimental Immunology and Imaging, University Hospital Essen) and were bred to *Ai9* mice to generate *Ly6G*^{TdTomato} mice, as reported previously⁴⁷. Experiments were performed in 8–20-week-old, age-matched male and female mice. Housing conditions followed a 12-hour dark/light cycle, room temperature of 18–22 °C and maintained humidity between 40% and 60%. Mice were fed with respective diets ad libitum. Wild-type controls were C57BL/6J, as recommended by the vendor, for studies in *Ccr2*^{-/-}, *CD36*^{-/-} and *Mertk*^{-/-} mice. To establish hypokalemia, mice consumed a potassium-deficient diet (background potassium: 15–30 p.p.m., TD.88239, Envigo) for 3 weeks. Macrophages were depleted by feeding mice a potassium-deficient diet containing *Csf1R* inhibitor PLX-5622 (1,200 p.p.m., MedChemExpress, and TD.200711, Envigo)⁴⁵. Neutrophils were depleted by injections of anti-Ly6G (BE0075-1, Bio X Cell) and mouse IgG2a anti-rat antibody (BE0122, Bio X Cell, each 100 µg d⁻¹, intraperitoneal (i.p.) for 3 days⁵⁰). Control mice were injected with IgG2a isotype control antibodies (BE0085 and BE0089, both Bio X Cell). For activation of the Cre/loxP system in hemizygous *Cx3cr1*^{CreEP}, mice received tamoxifen-containing diet for 10 days (500 mg kg⁻¹ diet, Td.130857, Envigo). Cre-carrying littermate controls were subjected to the same tamoxifen regimen as inducible knockouts. Where appropriate, animals were randomly assigned to experimental groups.

Telemeter implantation. For ETA-F10 transmitter (DSI) implantation, mice received buprenorphine (0.05 mg kg⁻¹ of body weight, i.p. injection) before the procedure. Mice were anesthetized by inhalation of 2% isoflurane. An abdominal incision allowed insertion of a sterile ETA-F10 telemetry device (DSI). The ECG leads were fixed in a modified lead II position. Buprenorphine treatment was continued twice daily for 3 days after implantation.

MI. MI was induced by permanent ligation of the left coronary artery. Mice were anesthetized with 2% isoflurane, intubated and mechanically ventilated. A left

thoracotomy was performed at the fourth intercostal space. The coronary artery was ligated with a monofilament nylon 8-0 suture (Ethicon). Animals were given buprenorphine before and twice daily for 3 days after MI.

Electrophysiological studies. An octapolar catheter (EPR-800, Millar) was inserted into the right jugular vein and positioned in the right atrium and ventricle. Ventricular effective refractory periods were measured using electrical stimulation with overdrive pacing trains at 100 ms, followed by single extra-stimuli. Ventricular arrhythmia induction was performed with triple extra-stimuli and pacing at gradually faster rates to a pacing cycle length of 10 ms.

Electrolyte measurements. Whole blood was centrifuged at 800g for 10 minutes at room temperature, and the K⁺, Cl⁻ and Na⁺ plasma levels were measured using a DRI-CHEM 7000 analyzer (Heska). For pH and iCa²⁺ measurements, blood was analyzed with an i-STAT CG4+ Cartridge (Patterson Veterinary Supply) using an i-STAT 1 system (FUSO Pharmaceutical Industries).

Bone marrow transplantation. Mice were lethally irradiated with a 9.5-Gy single shot. One day later, 5×10^6 bone marrow cells were transplanted via intravenous injection.

Flow cytometry and cell sorting. Heart tissue was minced and enzymatically digested using collagenase I (450 U ml⁻¹), collagenase XI (60 U ml⁻¹), DNase and hyaluronidase (60 U ml⁻¹) (Sigma-Aldrich). Single-cell suspensions were stained with CD45-PerCP/Cy5.5 (clone 30-F11, 1:600, 103132, BioLegend), CD64-APC (clone X54-5/7.1, 1:600, 139305, BioLegend), Ly6G-PE/Cy7 (clone 1A8, 1:600, 127617, BioLegend), Ly6C-FITC (clone HK1.4, 1:600, 128006, BioLegend), CD11b-BV510 (clone M1/70, 1:600, 101245, BioLegend) and DAPI (0.1%, F10347, Thermo Fisher Scientific). Blood samples from *Ly6G*^{TdTomato} mice were stained with Ly6G-PE/Cy7 (clone 1A8, 1:600, 127617, BioLegend), CD115-BV605 (clone AFS98, 1:600, 135517, BioLegend), CD11b-APC (clone M1/70, 1:600, 101212, BioLegend), CD45-BV711 (30-F11, 1:600, 103147, BioLegend), CD3-APC/Cy7 (clone 17A2, 1:200, 100221, BioLegend), CD19-APC/Cy7 (clone 6D5, 1:300, 115529, BioLegend), B220-APC/Cy7 (clone RA3-6B2, 1:300, 103224, BioLegend), Nk1.1-APC/Cy7 (clone PK136, 1:300, 108724, BioLegend) and DAPI. Data were recorded on an LSRII flow cytometer with FACSDiva 6.1 and analyzed with FlowJo 10 software (BD Biosciences). For qRT-PCR measurements, cells were flow sorted on a FACSAria II (BD Biosciences) into 350 µl of lysis buffer (RNeasy Plus Micro Kit, Qiagen).

Echocardiography. Echocardiography was performed using a MX250s transducer (15–30 MHz, center transmit: 21 MHz, axial resolution: 75 µm) together with a Vevo 3100 Imaging System (FUJIFILM VisualSonics)⁶⁰ during 2% isoflurane anesthesia.

Confocal microscopy of the isolated heart. *Myh6-GCaMP8* mice were retro-orbitally injected with anti-Ly6G-AP647 (clone 1A8, 127610, BioLegend) 30 minutes before MI induction. The excised heart was cannulated using an 18-gauge cannula and a 6-0 silk suture. After perfusion of the heart with pre-warmed KH buffer (NaHCO₃: 25 mM, KH₂PO₄: 1.2 mM, C₆H₁₂O₆: 11.1 mM, MgSO₄: 1.2 mM, KCl: 4.7 mM, NaCl: 118 mM, CaCl₂: 2.55 mM), a pacing wire was sutured to the left ventricular tissue for pacing at 8 Hz. To identify the infarct border zone, we used 5,000 blood flow determination beads (FluoSpheres Polystyrene Microspheres, F8891, Thermo Fisher Scientific). Data were acquired with a confocal microscope (FV1000-MPE, Olympus)⁷⁰.

FRI. Mice were intravenously injected with Annexin-V750 (250 µl, PerkinElmer) 4 hours after MI, 1 hour before imaging. Image acquisition was done using an epifluorescence microscope (OV-110, Olympus) equipped with IV10-ASW 01.01.00.05 software with an image matrix of 512 × 512 and 0.0178 mm × 0.0178 mm pixels. Mice were intravenously injected with TMRE perchlorate (1.5 µl of a 10 mM stock solution diluted in PBS, MedChemExpress) 4.5 hours after MI induction. Carbonyl cyanide 4-(trifluoromethoxy) phenylhydrazone (FCCP, 5 µl diluted in 150 µl of PBS, MedChemExpress) was retro-orbitally injected 15 minutes before TMRE. Oxidative stress was imaged after intravenous injection of CellROX Deep Red Reagent (C10422, Thermo Fisher Scientific, 20 µl diluted in 100 µl of PBS). Hearts were sliced in 1-mm sections for immediate imaging using a Sapphire Biomolecular Imager (Azure Biosystems).

Immunostaining. Hearts were embedded in OCT (Thermo Fisher Scientific). For TUNEL, sections were stained with In Situ Cell Death Detection Kit, TMR red (12156792910, Sigma-Aldrich), anti-cardiac troponin I antibody (ab47003, Abcam, 1:250) and a goat anti-rabbit IgG secondary antibody Alexa Fluor 488 conjugate (A-11034, Thermo Fisher Scientific, 1:100). Nuclei were counterstained with DAPI (D21490, Thermo Fisher Scientific, 1:3,000). Images were acquired with a digital slide scanner NanoZoomer 2.0RS (Hamamatsu). We harvested hearts from hypokalemic mTmG-*Myh6*^{Cre} reporter mice 5 hours after MI, and paraffin-embedded tissue sections were stained with Tom20 (D8T4N) rabbit monoclonal antibody (42406, Cell Signaling Technology, 1:50) for mitochondria, GFP antibody (ab13970, Abcam, 1:400) for cardiomyocytes and purified rat anti-mouse CD107b

(M3/84) (550292, BD Biosciences, 1:25, Mac-3) for macrophages, followed by goat anti-rabbit IgG Alexa Fluor 647 conjugate (A-21245, Thermo Fisher Scientific, 1:100), goat anti-chicken IgG Alexa Fluor 488 conjugate (A-11039, Thermo Fisher Scientific, 1:100) and goat anti-rat IgG Alexa Fluor 555 conjugate (A-21434, Thermo Fisher Scientific, 1:100). Images were acquired using an Olympus FV3000 system with a $\times 60$ oil immersion imaging objective (UPLAPO60XOHR). To measure infarct size, slices were stained with a 2% 2,3,5-triphenyltetrazolium chloride solution (Sigma-Aldrich) and imaged with a flatbed scanner.

TEM. Specimens were excised from the infarct core and fixed in 2% paraformaldehyde/2.5% glutaraldehyde in 0.1 M cacodylate buffer, rinsed in 0.1 M cacodylate buffer and infiltrated in 1% osmium tetroxide. Samples were transferred into a 1:1 mix of propylene oxide and eponate resin. Then, 70-nm sections were cut using a Leica EM UC7 ultramicrotome, collected onto formvar-coated grids, stained with 2% uranyl acetate and Reynold's lead citrate and examined in a JEOL JEM 1011 transmission electron microscope at 80 kV.

RNA isolation and real-time PCR. RNA was isolated with the RNeasy Mini Kit (74104, Qiagen) and the Plus Micro Kit (74034, Qiagen). High-Capacity RNA-to-cDNA Kit (4387406, Applied Biosystems) was used for reverse transcription. TaqMan gene expression assays were used with TaqMan Fast Universal PCR Master Mix (4366072, Applied Biosystems) and primers for Lcn2 (Mm01324470_m1), Casp3 (Mm01195085_m1), Mertk (Mm00434920_m1), Cd36 (Mm00432403_m1), Retnlg (Mm01346434_m1), Hdc (Mm00456104_m1), Fadd (Mm00438861_m1), Mlk1 (Mm01244222_m1), Tradd (Mm01251029_m1) and Gapdh (Mm99999915_g1, VIC-MGB, Thermo Fisher Scientific). Samples were run on a 7500 Real-Time PCR System (Applied Biosystems), and target gene expression was normalized to Gapdh.

Troponin ELISA. Whole blood was centrifuged for 10 minutes at 800 g, and the supernatant was analyzed using the Mouse Cardiac Troponin T ELISA Kit (MBS034636, MyBioSource).

Enzyme activity assays. For a Caspase-3 Assay Kit (ab39401, Abcam), infarct tissue was immersed in 400 µl of lysis buffer and disrupted using a homogenizer. To measure mitochondrial enzyme activities, we used the Complex II Enzyme Activity Microplate Assay Kit (ab109908, Abcam) and Complex IV Rodent Enzyme Activity Microplate Assay Kit (ab109911, Abcam).

Telemetry analyses. ECG recordings were analyzed using LabChart 8 (ADInstruments). VT were defined as (i) four or more consecutive broad QRS complexes of ventricular origin at a rate of >800 beats per minute, (ii) absence of the intrinsic QRS complex and (iii) dissociated or indistinguishable atrial activity⁷¹. Vfib was defined as disorganized electrical activity at a high rate, with pronounced variability in ECG waveform, peak–peak interval and height⁷¹. Incidence analysis included all mice in respective cohorts. For the analysis of VT and Vfib burden, we measured the cumulative time that mice spent in respective arrhythmia during the first 24 hours after MI. After clinical guidelines for atrial fibrillation^{72–74}, as VT burden and Vfib burden are not commonly assessed, we included mice that had a VT or Vfib >0 seconds in the burden analyses. QTc was assessed in at least five cardiac cycles per mouse⁷⁵.

Analyses of EP studies. Data from EP studies were analyzed using LabChart 8 Pro. All VTs <1 second were excluded.

Echocardiography analyses. Left ventricular volumes, ejection fraction and cardiac output were calculated from B-mode images using the semi-automated LVtrace-tool of Vevo LAB version 3.1.0 (FUJIFILM VisualSonics). All B-mode loops were traced twice to account for inter-beat variability. Peak velocities for E and A were assessed from pulsed-wave Doppler transmittal flow patterns and e' from tissue Doppler profiles of five peaks.

Analyses of confocal microscopy. To identify regions of interest with Ca²⁺ hotspots, cine loops were cropped into series of 5–30 frames using ImageJ 1.8.0_172. A dyssynchrony map was generated by plotting the standard deviation (s.d.) of GFP indicating cytosolic Ca concentration over the length of the respective time series. This dyssynchrony map was used to define Ca²⁺ hotspots with the ImageJ plugin SparkMaster⁷⁶ using a threshold of four times the s.d. The dyssynchrony map was merged with the AF-647 channel, and the distance from Ca²⁺ hotspots to neutrophils was quantified. Random spots were picked in each dyssynchrony map by using the Microsoft Excel function ‘randombetw’.

Analyses of FRI. Background mean fluorescent intensity (MFI) was determined by placing a region of interest (ROI) in the remote tissue with ImageJ 1.8.0_172. Annexin V-positive area was defined as MFI times $5 \times$ s.d. of remote cardiac tissue. Annexin V-positive areas were thresholded, and the ROI was placed into the infarct area to determine target MFI. Background MFI and target MFI from individual cardiac slices were used to calculate the TBR. For analyses of mitochondrial membrane potential, background MFI was determined adjacent to

tissue. Target ROIs were defined in the myocardium or in the infarct. Background MFI and target MFI from individual cardiac slices were used to calculate the TBR. Fluorescence intensity levels were displayed using a pseudo rainbow color scheme (OsiriX, Pixmeo SARL).

RNA-seq analysis. We analyzed deposited scRNA-seq data (GSE157244) consisting of immune cells isolated from infarcted murine hearts at day 1 ($n=3$ mice; 8,687 cells), day 2 ($n=3$ mice; 6,350 cells) and day 4 ($n=8$ mice, 20,843 cells) after permanent left anterior descending ligation¹³. Analyses were performed with R package Seurat version 3. Count matrices were merged into a single unified dataset and filtered to remove cells with unique molecular identifier counts below 100. Normalization, scaling, variable feature selection and principal component analysis-based dimensional reduction were performed with default parameters. Clustering was performed using the shared nearest neighbor clustering algorithm with the Louvain method for modularity optimization, as implemented in the Seurat FindNeighbors and FindClusters functions. Differentially expressed genes between clusters were determined using a Wilcoxon rank-sum test.

Histology data analyses. To analyze TUNEL staining, ten FOVs per animal from the infarct were exported at $\times 40$ using NanoZoomer NDPview2 software (Hamamatsu). For each FOV, we manually counted troponin⁺ DAPI⁺ TUNEL⁺ cardiomyocytes using ImageJ 1.8.0_172. Infarct size was quantified using ImageJ 1.8.0_172.

TEM data analyses. Images of TEM samples were taken by a blinded observer using an AMT digital imaging system with proprietary image capture software (Advanced Microscopy Techniques). We used ImageJ 1.8.0_172 to quantify (i) mitochondria per FOV from images with $\times 8,000$ magnification, (ii) mitochondrial area from FOVs with $\times 25,000$ magnification, (iii) cristae and (iv) and paracrystalline inclusions from images with $\times 40,000$ magnification. Free extracellular mitochondria were defined as mitochondria not separated by a cell membrane from the extracellular space.

Statistical tests. Statistical analyses were performed using GraphPad Prism 9. Results are reported as mean \pm s.e.m. Normality was assessed using the Shapiro-Wilk normality test. For a two-group comparison, normally distributed datasets underwent an unpaired parametric two-tailed *t*-test, whereas non-normally distributed data were evaluated with a non-parametric two-tailed Mann-Whitney test. For multiple comparisons, we used an ANOVA followed by a Tukey's post test or test for linear trend as appropriate. For a description of the statistical methods used for the human studies, see the relevant Methods section 'Human subjects'.

Reporting summary. Further information on research design is available in the Nature Research Reporting Summary linked to this article.

Data availability

The scRNA-seq data were previously deposited in the National Center of Biotechnology Information's Gene Expression Omnibus and are accessible through accession number GSE157244 (K.R.K.). Additional data supporting the findings in this study are included in the main article and associated files. Source data are provided with this paper.

Code availability

This manuscript does not report original code.

Received: 15 December 2021; Accepted: 6 June 2022;

Published online: 11 July 2022

References

- Chugh, S. S. et al. Current burden of sudden cardiac death: multiple source surveillance versus retrospective death certificate-based review in a large U.S. community. *J. Am. Coll. Cardiol.* **44**, 1268–1275 (2004).
- Borne, R. T., Varosy, P. D. & Masoudi, F. A. Implantable cardioverter-defibrillator shocks: epidemiology, outcomes, and therapeutic approaches. *JAMA Intern. Med.* **173**, 859–865 (2013).
- Bhar-Amato, J., Davies, W. & Agarwal, S. Ventricular arrhythmia after acute myocardial infarction: 'the perfect storm'. *Arrhythm. Electrophysiol. Rev.* **6**, 134–139 (2017).
- Suga, H. Ventricular energetics. *Physiol. Rev.* **70**, 247–277 (1990).
- Brown, D. A. & O'Rourke, B. Cardiac mitochondria and arrhythmias. *Cardiovasc. Res.* **88**, 241–249 (2010).
- Campos, F. O. et al. Factors promoting conduction slowing as substrates for block and reentry in infarcted hearts. *Biophys. J.* **117**, 2361–2374 (2019).
- Pinto, A. R. et al. Revisiting cardiac cellular composition. *Circ. Res.* **118**, 400–409 (2016).
- Litvinčuková, M. et al. Cells of the adult human heart. *Nature* **588**, 466–472 (2020).
- Hulsmans, M. et al. Macrophages facilitate electrical conduction in the heart. *Cell* **169**, 510–522 (2017).

10. Nicolás-Ávila, J. A. et al. A network of macrophages supports mitochondrial homeostasis in the heart. *Cell* **183**, 94–109 (2020).
11. Frodermann, V. & Nahrendorf, M. Macrophages and cardiovascular health. *Physiol. Rev.* **98**, 2523–2569 (2018).
12. Kaese, S. & Verheule, S. Cardiac electrophysiology in mice: a matter of size. *Front. Physiol.* **3**, 345 (2012).
13. Ravn Jacobsen, M. et al. Potassium disturbances and risk of ventricular fibrillation among patients with ST-segment-elevation myocardial infarction. *J. Am. Heart Assoc.* **9**, e014160 (2020).
14. Ohlow, M.-A. et al. Incidence and predictors of ventricular arrhythmias after ST-segment elevation myocardial infarction. *Am. J. Emerg. Med.* **30**, 580–586 (2012).
15. Rahimi, K. et al. Incidence, time course, and predictors of early malignant ventricular arrhythmias after non-ST-segment elevation myocardial infarction in patients with early invasive treatment. *Eur. Heart J.* **27**, 1706–1711 (2006).
16. Lindsey, M. L., Kassiri, Z., Virag, J. A. I., de Castro Brás, L. E. & Scherrer-Crosbie, M. Guidelines for measuring cardiac physiology in mice. *Am. J. Physiol. Heart Circ. Physiol.* **314**, H733–H752 (2018).
17. Boivin, G. et al. Durable and controlled depletion of neutrophils in mice. *Nat. Commun.* **11**, 2762 (2020).
18. Opitz, C. F., Mitchell, G. F., Pfeffer, M. A. & Pfeffer, J. M. Arrhythmias and death after coronary artery occlusion in the rat. Continuous telemetric ECG monitoring in conscious, untethered rats. *Circulation* **92**, 253–261 (1995).
19. Solomon, S. D. et al. Sudden death in patients with myocardial infarction and left ventricular dysfunction, heart failure, or both. *N. Engl. J. Med.* **352**, 2581–2588 (2005).
20. Jeong, E.-M. et al. Metabolic stress, reactive oxygen species, and arrhythmia. *J. Mol. Cell. Cardiol.* **52**, 454–463 (2012).
21. Calcagno, D. M. et al. The myeloid type I interferon response to myocardial infarction begins in bone marrow and is regulated by Nrf2-activated macrophages. *Sci. Immunol.* **5**, eaaz1974 (2020).
22. Saha, P. et al. Bacterial siderophores hijack neutrophil functions. *J. Immunol.* **198**, 4293–4303 (2017).
23. Gu, Y., Geng, J., Xu, Z., Chen, Y. & Zhang, X.-W. Neutrophil gelatinase-associated lipocalin2 exaggerates cardiomyocyte hypoxia injury by inhibiting integrin β 3 signaling. *Med. Sci. Monit.* **25**, 5426–5434 (2019).
24. Song, E. et al. Holo-lipocalin-2-derived siderophores increase mitochondrial ROS and impair oxidative phosphorylation in rat cardiomyocytes. *Proc. Natl Acad. Sci. USA* **115**, 1576–1581 (2018).
25. Lindberg, S. et al. Prognostic utility of neutrophil gelatinase-associated lipocalin in predicting mortality and cardiovascular events in patients with ST-segment elevation myocardial infarction treated with primary percutaneous coronary intervention. *J. Am. Coll. Cardiol.* **60**, 339–345 (2012).
26. Nahrendorf, M. et al. The healing myocardium sequentially mobilizes two monocyte subsets with divergent and complementary functions. *J. Exp. Med.* **204**, 3037–3047 (2007).
27. Lei, F. et al. CSF1R inhibition by a small-molecule inhibitor is not microglia specific; affecting hematopoiesis and the function of macrophages. *Proc. Natl Acad. Sci. USA* **117**, 23336–23338 (2020).
28. Bajpai, G. et al. Tissue resident CCR2 $^{-}$ and CCR2 $^{+}$ cardiac macrophages differentially orchestrate monocyte recruitment and fate specification following myocardial injury. *Circ. Res.* **124**, 263–278 (2019).
29. Daseke, M. J. et al. Exogenous IL-4 shuts off pro-inflammation in neutrophils while stimulating anti-inflammation in macrophages to induce neutrophil phagocytosis following myocardial infarction. *J. Mol. Cell. Cardiol.* **145**, 112–121 (2020).
30. Hasenberg, A. et al. Catchup: a mouse model for imaging-based tracking and modulation of neutrophil granulocytes. *Nat. Methods* **12**, 445–452 (2015).
31. DeBerge, M. et al. MerTK cleavage on resident cardiac macrophages compromises repair after myocardial ischemia reperfusion injury. *Circ. Res.* **121**, 930–940 (2017).
32. Wan, E. et al. Enhanced efferocytosis of apoptotic cardiomyocytes through myeloid-epithelial-reproductive tyrosine kinase links acute inflammation resolution to cardiac repair after infarction. *Circ. Res.* **113**, 1004–1012 (2013).
33. Laufer, E. M., Reutelingsperger, C. P. M., Narula, J. & Hofstra, L. Annexin A5: an imaging biomarker of cardiovascular risk. *Basic Res. Cardiol.* **103**, 95–104 (2008).
34. Ramachandra, C. J. A., Hernandez-Resendiz, S., Crespo-Avilan, G. E., Lin, Y.-H. & Hausenloy, D. J. Mitochondria in acute myocardial infarction and cardioprotection. *EBioMedicine* **57**, 102884 (2020).
35. Bryant, R. E., Thomas, W. A. & O'Neal, R. M. An electron microscopic study of myocardial ischemia in the rat. *Circ. Res.* **6**, 699–709 (1958).
36. Stadhouders, A. M., Jap, P. H., Winkler, H. P., Eppenberger, H. M. & Wallimann, T. Mitochondrial creatine kinase: a major constituent of pathological inclusions seen in mitochondrial myopathies. *Proc. Natl Acad. Sci. USA* **91**, 5089–5093 (1994).
37. Nunnari, J. & Suomalainen, A. Mitochondria: in sickness and in health. *Cell* **148**, 1145–1159 (2012).
38. Ricci, J.-E., Gottlieb, R. A. & Green, D. R. Caspase-mediated loss of mitochondrial function and generation of reactive oxygen species during apoptosis. *J. Cell Biol.* **160**, 65–75 (2003).
39. Dedkova, E. N. & Blatter, L. A. Measuring mitochondrial function in intact cardiac myocytes. *J. Mol. Cell. Cardiol.* **52**, 48–61 (2012).
40. Canton, J., Neculai, D. & Grinstein, S. Scavenger receptors in homeostasis and immunity. *Nat. Rev. Immunol.* **13**, 621–634 (2013).
41. Dehn, S. & Thorp, E. B. Myeloid receptor CD36 is required for early phagocytosis of myocardial infarcts and induction of Nr4a1-dependent mechanisms of cardiac repair. *FASEB J.* **32**, 254–264 (2018).
42. Kohl, P., Kamkin, A. G., Kiseleva, I. S. & Noble, D. Mechanosensitive fibroblasts in the sino-atrial node region of rat heart: interaction with cardiomyocytes and possible role. *Exp. Physiol.* **79**, 943–956 (1994).
43. Bajpai, G. et al. The human heart contains distinct macrophage subsets with divergent origins and functions. *Nat. Med.* **24**, 1234–1245 (2018).
44. Grune, J., Yamazoe, M. & Nahrendorf, M. Electroimmunology and cardiac arrhythmia. *Nat. Rev. Cardiol.* **18**, 547–564 (2021).
45. Francis Stuart, S. D., De Jesus, N. M., Lindsey, M. L. & Ripplinger, C. M. The crossroads of inflammation, fibrosis, and arrhythmia following myocardial infarction. *J. Mol. Cell. Cardiol.* **91**, 114–122 (2016).
46. Yao, C. et al. Enhanced cardiomyocyte NLRP3 inflammasome signaling promotes atrial fibrillation. *Circulation* **138**, 2227–2242 (2018).
47. Rudolph, V. et al. Myeloperoxidase acts as a profibrotic mediator of atrial fibrillation. *Nat. Med.* **16**, 470–474 (2010).
48. Epelman, S. et al. Embryonic and adult-derived resident cardiac macrophages are maintained through distinct mechanisms at steady state and during inflammation. *Immunity* **40**, 91–104 (2014).
49. Boukens, B. J. D., Christoffels, V. M., Coronel, R. & Moorman, A. F. M. Developmental basis for electrophysiological heterogeneity in the ventricular and outflow tract myocardium as a substrate for life-threatening ventricular arrhythmias. *Circ. Res.* **104**, 19–31 (2009).
50. Akar, F. G., Aon, M. A., Tomaselli, G. F. & O'Rourke, B. The mitochondrial origin of postischemic arrhythmias. *J. Clin. Invest.* **115**, 3527–3535 (2005).
51. Sciarretta, S., Maejima, Y., Zablocki, D. & Sadoshima, J. The role of autophagy in the heart. *Annu. Rev. Physiol.* **80**, 1–26 (2018).
52. Sugita, J. et al. Cardiac macrophages prevent sudden death during heart stress. *Nat. Commun.* **12**, 1910 (2021).
53. Herring, N., Kalla, M. & Paterson, D. J. The autonomic nervous system and cardiac arrhythmias: current concepts and emerging therapies. *Nat. Rev. Cardiol.* **16**, 707–726 (2019).
54. Nahrendorf, M. Myeloid cell contributions to cardiovascular health and disease. *Nat. Med.* **24**, 711–720 (2018).
55. De Jesus, N. M. et al. Atherosclerosis exacerbates arrhythmia following myocardial infarction: role of myocardial inflammation. *Heart Rhythm* **12**, 169–178 (2015).
56. Clauss, S. et al. Animal models of arrhythmia: classic electrophysiology to genetically modified large animals. *Nat. Rev. Cardiol.* **16**, 457–475 (2019).
57. Horckmans, M. et al. Neutrophils orchestrate post-myocardial infarction healing by polarizing macrophages towards a reparative phenotype. *Eur. Heart J.* **38**, 187–197 (2017).
58. Phillipson, M. & Kubes, P. The healing power of neutrophils. *Trends Immunol.* **40**, 635–647 (2019).
59. Mook-Kanamori, B. B., Geldhoff, M., van der Poll, T. & van de Beek, D. Pathogenesis and pathophysiology of pneumococcal meningitis. *Clin. Microbiol. Rev.* **24**, 557–591 (2011).
60. van de Beek, D., de Gans, J., Tunkel, A. R. & Wijdicks, E. F. M. Community-acquired bacterial meningitis in adults. *N. Engl. J. Med.* **354**, 44–53 (2006).
61. Alkhail, M. et al. Hyper-acute cardiovascular magnetic resonance T1 mapping predicts infarct characteristics in patients with ST elevation myocardial infarction. *J. Cardiovasc. Magn. Reson.* **22**, 3 (2020).
62. Kalla, M. et al. The cardiac sympathetic co-transmitter neuropeptide Y is pro-arrhythmic following ST-elevation myocardial infarction despite beta-blockade. *Eur. Heart J.* **41**, 2168–2179 (2020).
63. Piechnik, S. K. et al. Shortened Modified Look-Locker Inversion recovery (ShMOLLI) for clinical myocardial T1-mapping at 1.5 and 3 T within a 9 heartbeat breathhold. *J. Cardiovasc. Magn. Reson.* **12**, 69 (2010).
64. Daniel, W. W. *Applied Nonparametric Statistics* (Duxbury, 1990).
65. Seshan, V. E. & Whiting, K. Package 'clinfun': Clinical Trial Design and Data Analysis Functions. Version 1.1.0. <https://cran.r-project.org/web/packages/clinfun/clinfun.pdf> (2022).
66. Gorenek, B. et al. Cardiac arrhythmias in acute coronary syndromes: position paper from the joint EHRA, ACCA, and EAPCI task force. *Eur. Heart J. Acute Cardiovasc. Care* **4**, 386 (2015).
67. Grambsch, P. M. & Therneau, T. M. Proportional hazards tests and diagnostics based on weighted residuals. *Biometrika* **81**, 515–526 (1994).
68. Therneau, T. A Package for Survival Analysis in R. <https://cran.r-project.org/package=survival> (2020).
69. Grune, J. et al. Selective mineralocorticoid receptor cofactor modulation as molecular basis for Finerenone's antifibrotic activity. *Hypertension* **71**, 599–608 (2018).

70. Aguirre, A. D., Vinegoni, C., Sebas, M. & Weissleder, R. Intravital imaging of cardiac function at the single-cell level. *Proc. Natl Acad. Sci. USA* **111**, 11257–11262 (2014).
71. Curtis, M. J. et al. The Lethbridge Conventions (II): guidelines for the study of animal and human ventricular and supraventricular arrhythmias. *Pharmacol. Ther.* **139**, 213–248 (2013).
72. Chen, L. Y. et al. Atrial fibrillation burden: moving beyond atrial fibrillation as a binary entity: a scientific statement from the American Heart Association. *Circulation* **137**, e623–e644 (2018).
73. Gold, M. R. et al. Impact of atrial prevention pacing on atrial fibrillation burden: primary results of the Study of Atrial Fibrillation Reduction (SAFARI) trial. *Heart Rhythm* **6**, 295–301 (2009).
74. Brachmann, J. et al. Atrial Fibrillation Burden and Clinical Outcomes in Heart Failure: the CASTLE-AF Trial. *JACC Clin. Electrophysiol.* **7**, 594–603 (2021).
75. McCauley, M. D. et al. Pathogenesis of lethal cardiac arrhythmias in *Mecp2* mutant mice: implication for therapy in Rett syndrome. *Sci. Transl. Med.* **3**, 113ra125 (2011).
76. Picht, E., Zima, A. V., Blatter, L. A. & Bers, D. M. SparkMaster: automated calcium spark analysis with ImageJ. *Am. J. Physiol. Cell Physiol.* **293**, C1073–C1081 (2007).

Acknowledgements

This work was funded by NIH R21EB026762 (A.D.A) and HL144515 (A.D.A.). The authors thank V. Mootha and all Nahrendorf laboratory members for discussion and insightful ideas; the HSCI-CRM Flow Cytometry Core for assistance with cell sorting; K. Joyes for editing the manuscript; the Rothlin-Ghosh laboratory for providing Mertk^{-/-} mice; and the Microscopy Core of the Center for Systems Biology/Program in Membrane Biology, which is partially supported by Inflammatory Bowel Disease Grant DK043351 and Boston Area Diabetes and Endocrinology Research Center Award DK057521. This work was funded, in part, by US federal funds HL139598 (M.N.), HL142494 (M.N.), HL125428 (M.N.), HL155097 (M.H.), DP2AR075321 (K.R.K.) and NIH R00HL129168 (K.R.K.). J.G. and M.J.S. were funded by the German Research Foundation. J.G. was funded by DynAge FU Berlin, the German Society for Cardiology and the German Center for Cardiovascular Research. F.E.P. was funded by an F32 grant (HL158040). P.T.E. was supported by the NIH (1R01HL092577 and K24HL105780), by the American Heart Association (18SFRN34110082) and by MAESTRIA (965286). A.L., N.H., K.C. and S.N. acknowledge funding support from the British Heart Foundation Oxford Centre of Research Excellence. A.L. acknowledges funding support from the British Heart Foundation FS/TF/20/3300, the Academy of Medical Sciences SGL021\1038 and the NIHR Oxford Biomedical Research Centre. M.H. was supported by an American Heart Association Career Development Award (19CDA34490005). The graphical abstract was created with BioRender (publication license VB237K335B).

Oxford Acute Myocardial Infarction (OxAMI) Study

Mayooran Shanmuganathan^{21,22}, Vanessa M. Ferreira^{21,22} and Keith M. Channon^{21,22}

²¹Radcliffe Department of Medicine, University of Oxford, Oxford, UK. ²²National Institute for Health (NIHR) Biomedical Research Centre, Oxford University Hospitals NHS Foundation Trust, John Radcliffe Hospital, Oxford, UK.

Author contributions

J.G. conceived the study; designed, performed and analyzed experiments; interpreted data; and created the figures. A.J.M.L., M.Y., M.H., D.R., L.X., S.Z., C.O., Y.Z., K.T., M.S., F.P., M.J.S., D.C., G.W., Y.I. and A.D.A. performed experiments and collected data. M.S., B.F., J.H., N.H., V.M.F., S.N. and K.C. provided human specimens and data. D.M.C. and K.R.K. analyzed and processed RNA sequencing data. T.G., D.B., J.H., D.E.S., D.J.M., F.K.S., K.R.K., A.D.A., P.T.E. and M.N. discussed results and strategy. J.G. and M.N. wrote the manuscript, with input from all authors. M.N. conceived and directed the study.

Competing interests

J.G. and M.N. filed an invention disclosure on the STORM model. M.N. has received funds or material research support from Alnylam, Biotronik, CSL Behring, GlycoMimetics, GlaxoSmithKline, Medtronic, Novartis and Pfizer as well as consulting fees from Eli Lilly, Biogen, Gimv, IFM Therapeutics, Molecular Imaging, Sigilon and Verseau Therapeutics. P.T.E. has received sponsored research support from Bayer AG and IBM Health and has consulted for Bayer AG, Novartis and MyoKardia. A.D.A. has received sponsored research support from Amgen and Philip Research. The other authors declare no competing interests.

Additional information

Extended data is available for this paper at <https://doi.org/10.1038/s44161-022-00094-w>.

Supplementary information The online version contains supplementary material available at <https://doi.org/10.1038/s44161-022-00094-w>.

Correspondence and requests for materials should be addressed to Matthias Nahrendorf.

Peer review information *Nature Cardiovascular Research* thanks Andrés Hidalgo, Zhou Lan and the other, anonymous, reviewer(s) for their contribution to the peer review of this work.

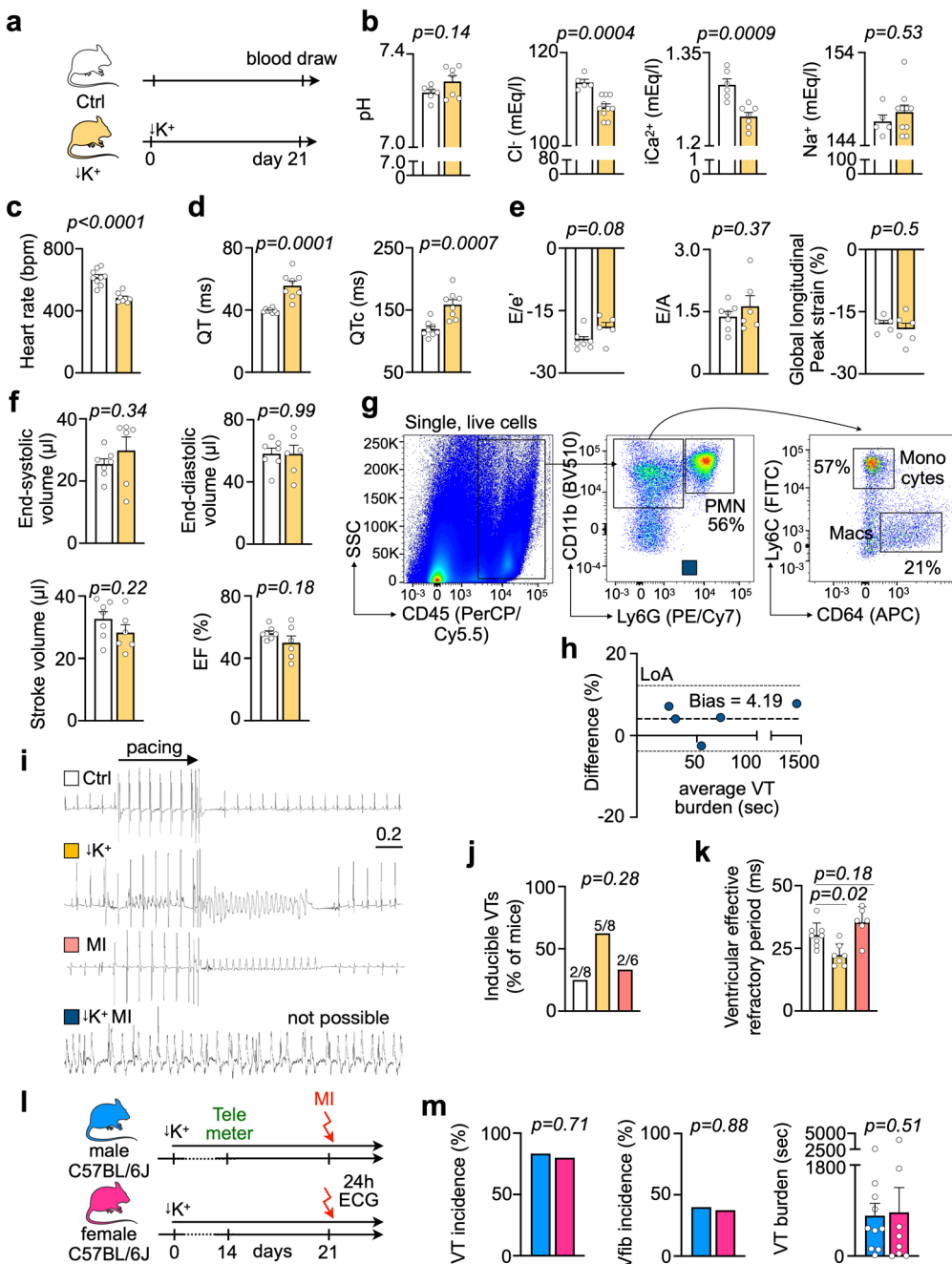
Reprints and permissions information is available at www.nature.com/reprints.

Publisher's note Springer Nature remains neutral with regard to jurisdictional claims in published maps and institutional affiliations.

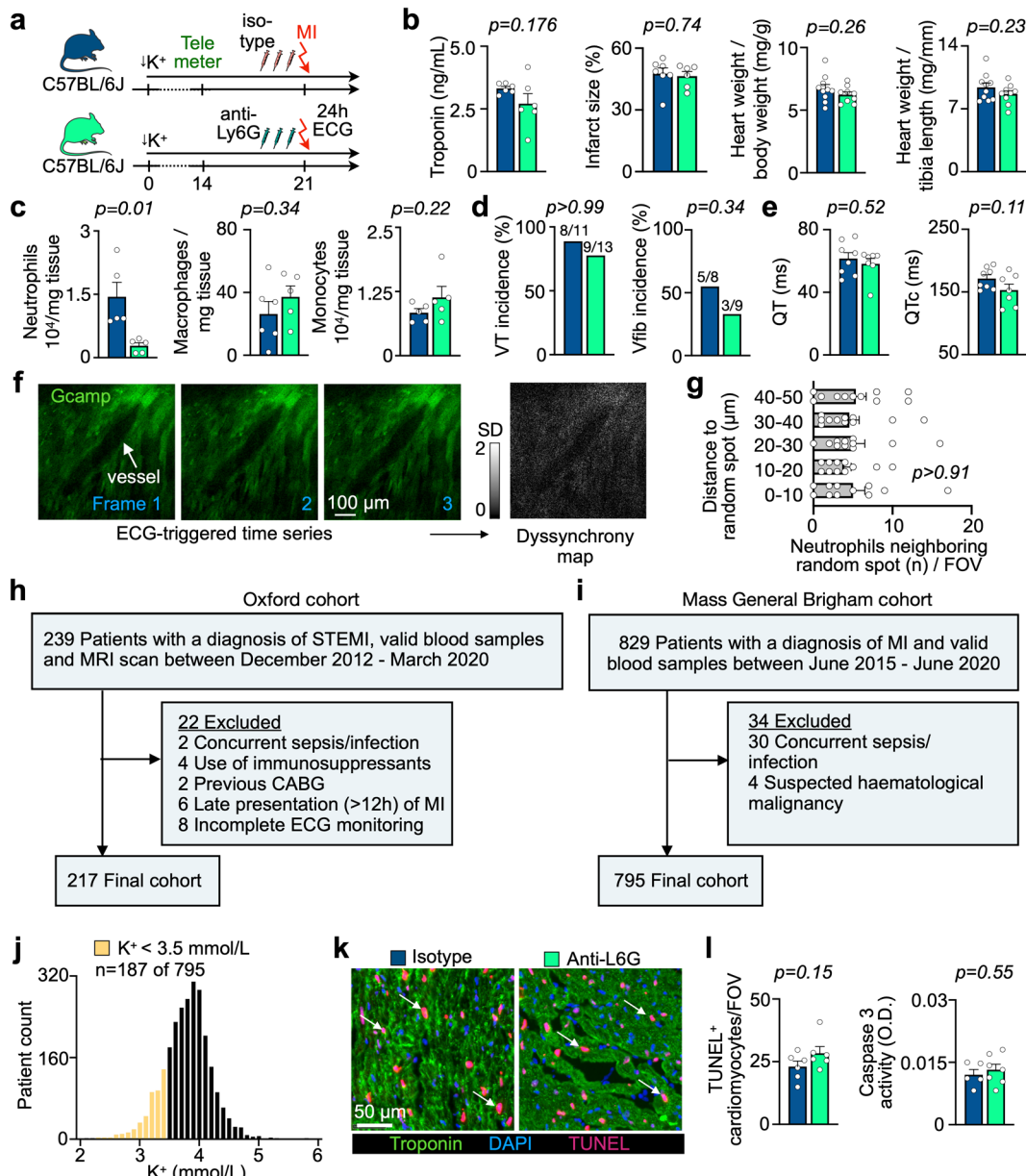


Open Access This article is licensed under a Creative Commons Attribution 4.0 International License, which permits use, sharing, adaptation, distribution and reproduction in any medium or format, as long as you give appropriate credit to the original author(s) and the source, provide a link to the Creative Commons license, and indicate if changes were made. The images or other third party material in this article are included in the article's Creative Commons license, unless indicated otherwise in a credit line to the material. If material is not included in the article's Creative Commons license and your intended use is not permitted by statutory regulation or exceeds the permitted use, you will need to obtain permission directly from the copyright holder. To view a copy of this license, visit <http://creativecommons.org/licenses/by/4.0/>.

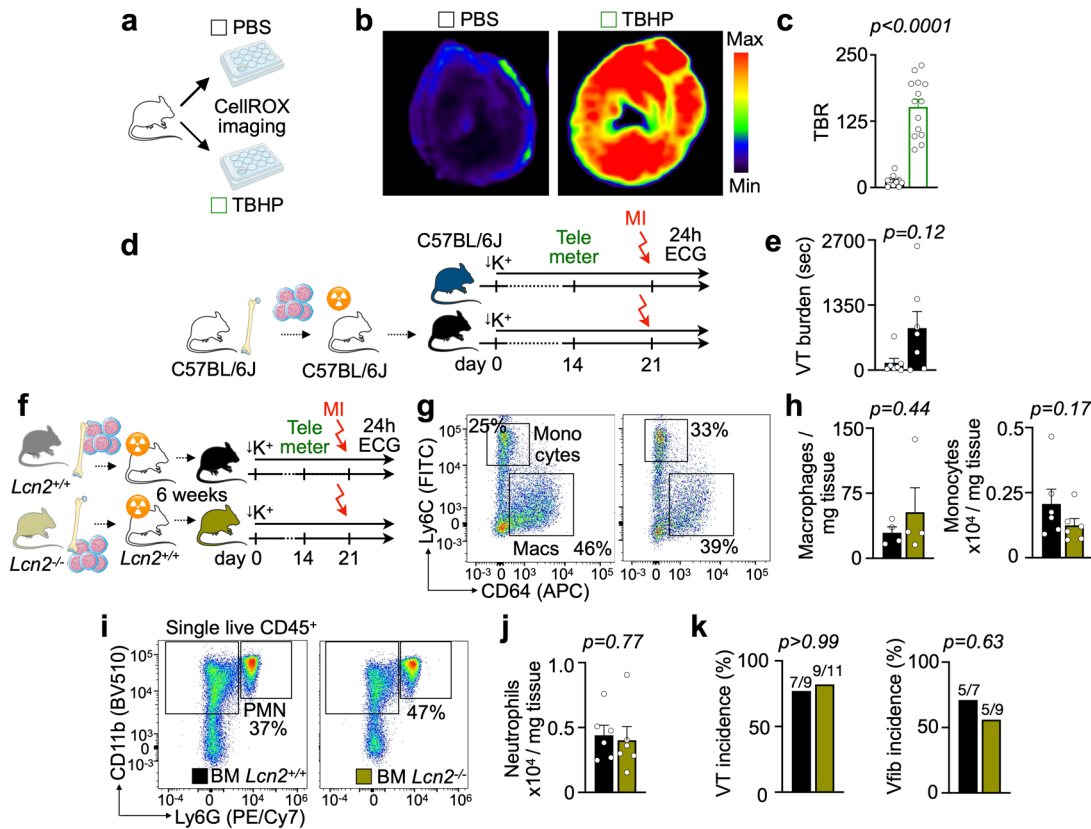
© The Author(s) 2022



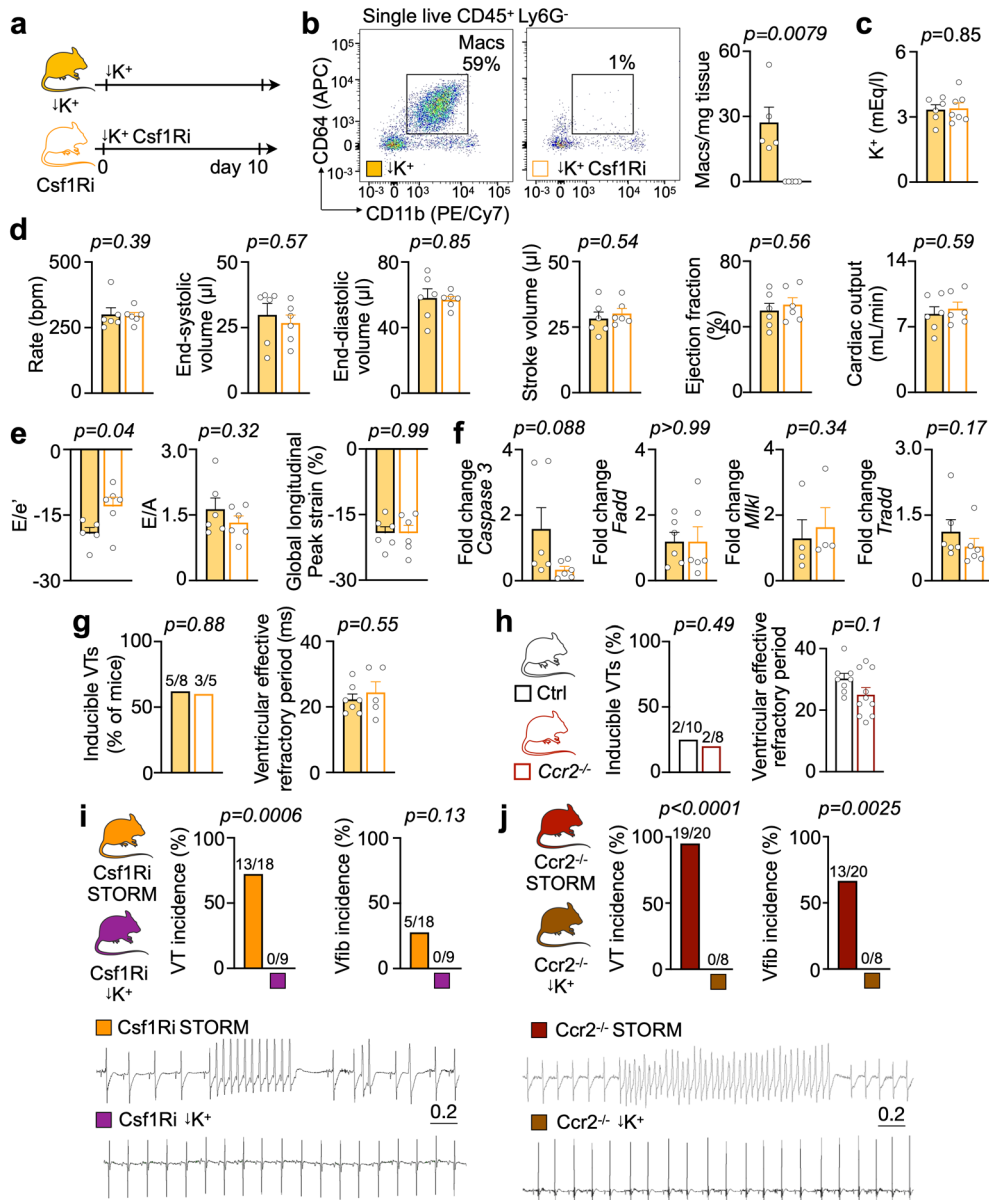
Extended Data Fig. 1 | Phenotyping hypokalemic mice. a, Experimental outline. b, pH, Cl^- , iCa^{2+} and Na^+ measured in normokalemic ($n=5$ or $n=6$ mice) and hypokalemic mice ($n=7$ or $n=10$). Two-sided unpaired t tests were used. c, Average heart rate by telemetric ECG recordings in ambulatory normokalemic ($n=9$ mice) and hypokalemic mice ($n=8$). Two-sided unpaired t tests were used. d, QT and QTc intervals in normokalemic ($n=8$ mice) and hypokalemic mice ($n=8$). Two-sided unpaired t tests were used. e, Diastolic function measured by echocardiography in normokalemic ($n=7$ mice) and hypokalemic ($n=5$ or $n=6$) mice indicated by the ratio between mitral inflow velocity and mitral valve annular early diastolic velocity (E/e'), late diastolic trans-mitral flow velocity (E/A) and global longitudinal peak strain (GLS). Two-sided unpaired t tests were used. f, Systolic function by echocardiography in normokalemic ($n=7$ mice) and hypokalemic ($n=6$) mice, indicated by end-systolic and end-diastolic left ventricular volumes, stroke volume and ejection fraction. Two-sided unpaired t tests were used. g, Gating strategy for cardiac leukocytes. h, Bland-Altman diagram demonstrating the difference of the ventricular tachycardia (VT) burden between two observers in percent. Dashed line: Bias. Dotted lines: Limits of Agreement (LoA). i, Representative ECG tracings from an invasive electrophysiological study. j, Inducibility of ventricular tachycardia (VT) after pacing in naive, hypokalemic and MI mice. Mouse numbers are indicated in plot. MI mice were measured 5 hrs after surgical induction. One-sided Chi-square test was used. k, Ventricular effective refractory period ($n=6$ or $n=8$ mice per group) in naive, hypokalemic and mice 5 hrs after MI. For STORM mice, catheter insertion caused spontaneous VTs which made an EP study impossible. One-way ANOVA followed by Tukey's multiple comparisons test were used. l, Experimental outline. m, Incidence of ventricular arrhythmias and VT burden in male ($n=10$ mice) and female ($n=8$) mice after STORM procedure. Fisher's exact test (VT and Vfib incidence) and two-sided Mann Whitney test (VT burden) were used. Data are mean \pm SEM.



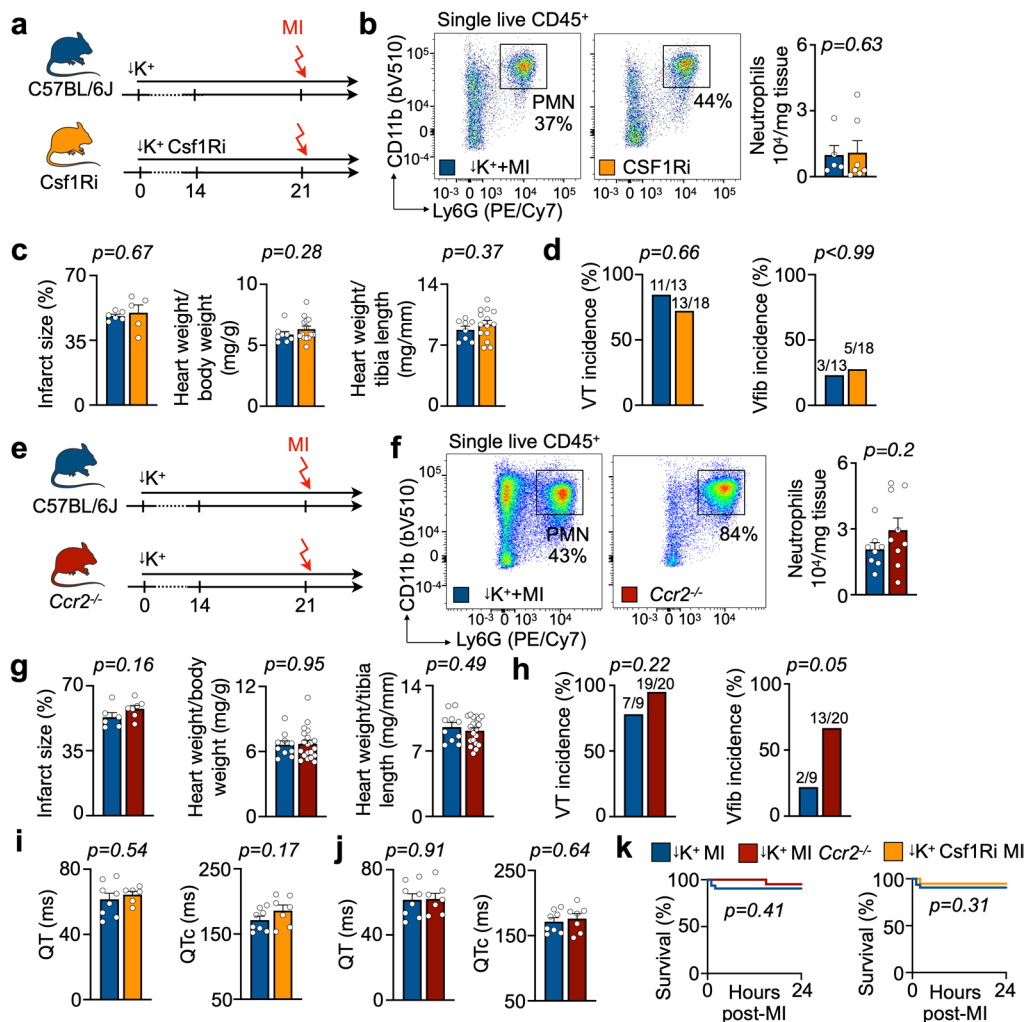
Extended Data Fig. 2 | Neutrophil depletion effects after MI. **a**, Experimental outline. **b**, Serum troponin, infarct size, heart weight-to-body weight ratio and heart weight-to-tibia length ratio from isotype-injected ($n=6$ or $n=10$ mice) and anti-Ly6G antibody-injected ($n=6$ or $n=9$ mice). Two-sided unpaired t tests were used. **c**, Flow cytometric quantification of cardiac macrophages in STORM mice undergoing isotype ($n=6$ mice) or anti-Ly6G antibody (neutrophil depletion, $n=5$ mice) injections after MI. Two-sided unpaired t test was used. **d**, Ventricular tachycardia (VT) incidence, ventricular fibrillation (Vfib) incidence (n-numbers indicated in plots) obtained by telemetric ECG recordings in ambulatory isotype-injected ($n=8$ mice) and anti-Ly6G-injected ($n=7$) mice, all after STORM exposure. Two-sided Fisher's exact tests was used. **e**, QT and QTc intervals assessed in STORM mice ($n=10$ mice) and STORM mice undergoing neutrophil depletion ($n=7$). Two-sided unpaired t tests were used. **f**, Confocal microscopy image of isolated Langendorff heart from a control *Myh6-GCaMP8* mouse. The ECG-triggered time series was used to calculate a dyssynchrony map (standard deviation of the Ca^{2+} channel (gcamp) over time). None were identified in this control experiment. Scale bar indicates 100 μm . This experiment was repeated independently four times. **g**, Distances from anti-Ly6G-labeled neutrophils to randomly distributed spots in individual fields of view (FOVs). Data were generated from $n=3$ mice and $n=11$ FOVs. Three random spots were assigned in each FOV and the distance to neutrophils closer than 50 μm was measured. One-way ANOVA was used. **h**, Exclusion chart for Oxford cohort. **i**, Exclusion chart for Mass General Brigham cohort. **j**, Serum potassium levels measured in MI patients ($n=795$) in the Mass General Brigham cohort. Data represent the lowest potassium level measured during hospitalization due to MI. **k**, TUNEL, troponin and DAPI staining of sections from the infarct 5 hrs after MI in STORM mice. Scale bar indicates 50 μm . **l**, Analysis of TUNEL⁺ cardiomyocytes/FOV and Caspase 3 activity (O.D.) measured in infarcted myocardium (5 hrs post MI) from isotype control antibody injected C57BL/6 mice ($n=6$ mice) and mice with neutrophil depletion treatment ($n=7$), all after STORM procedure. Two-sided unpaired t tests were used. Data are mean \pm SEM.



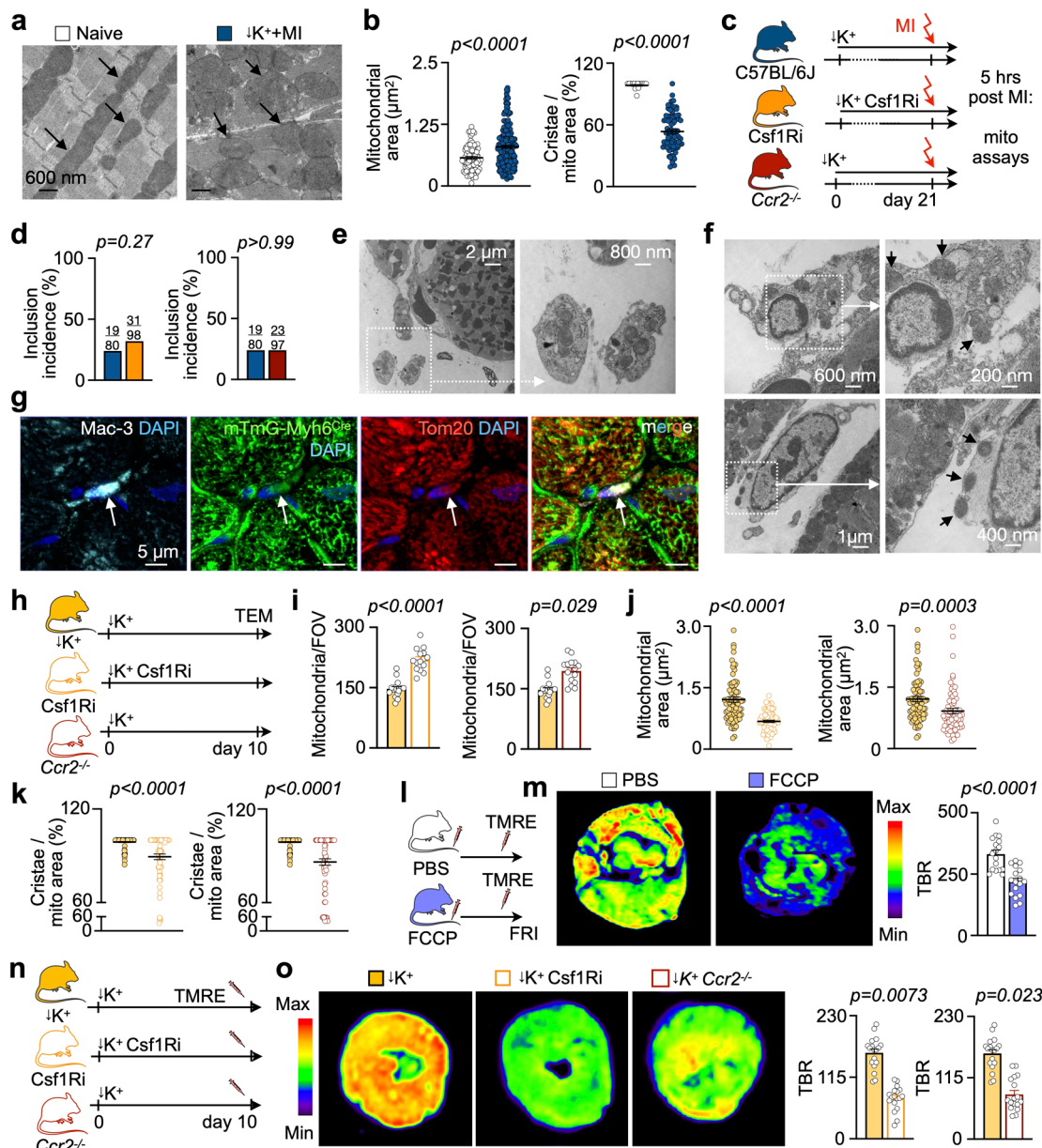
Extended Data Fig. 3 | *Lcn2* deletion in bone marrow cells. **a**, Experimental outline for CellROX validation. Mice were intravenously injected with CellROX. After 30 min, hearts were excised and cardiac slices were incubated either in PBS or a tert-butyl hydroperoxide (TBHP) solution that increases oxidative stress. **b**, Fluorescence images from cardiac short axis slices after intravenous injection of CellROX and incubation with either control PBS or TBHP. **c**, Quantification of target-to-background ratio (TBR) from FRI. Background mean fluorescence intensity was measured in the image background outside tissue. Data are from incubation with PBS ($n=4$ mice) or TBHP ($n=4$). Each dot represents a cardiac slice. Two-sided unpaired t test was used. **d**, Experimental outline. Lethal irradiation was followed by bone marrow transplantation and the STORM procedure. **e**, Ventricular tachycardia (VT) burden in mice without ($n=7$ mice) and with bone marrow transplantation ($n=7$), after STORM procedure. Two-sided Mann Whitney test was used. **f**, Experimental outline of bone marrow transplantation approach using wild type or *Lcn2*^{-/-} donor mice followed by STORM procedure. **g**, Flow plots of cardiac monocyte and macrophage populations in *Lcn2*^{+/+} and *Lcn2*^{-/-} bone marrow chimeras after STORM procedure, 5hrs after MI. **h**, Quantification of cardiac monocyte and macrophages in *Lcn2*^{+/+} ($n=6$ mice) and *Lcn2*^{-/-} bone marrow chimeras ($n=6$) after STORM protocol. Two-sided unpaired t tests were used. **i**, Flow plots of cardiac neutrophils (PMN) in *Lcn2*^{+/+} and *Lcn2*^{-/-} bone marrow chimeras after STORM procedure, 5hrs after MI. **j**, Quantification of cardiac monocyte and macrophages in *Lcn2*^{+/+} ($n=6$ mice) and *Lcn2*^{-/-} bone marrow chimeras ($n=6$) after STORM protocol. A Mann Whitney test (monocytes) and a two-sided unpaired t test (Macrophages) were used. **k**, Ventricular tachycardia (VT) incidence and ventricular fibrillation (Vfib) incidence (n -numbers indicated in plots) in ambulatory *Lcn2*^{+/+} ($n=7$ mice) and *Lcn2*^{-/-} bone marrow chimeras ($n=9$) after STORM procedure. Two-sided Fisher's exact tests were used. Data are mean \pm SEM.



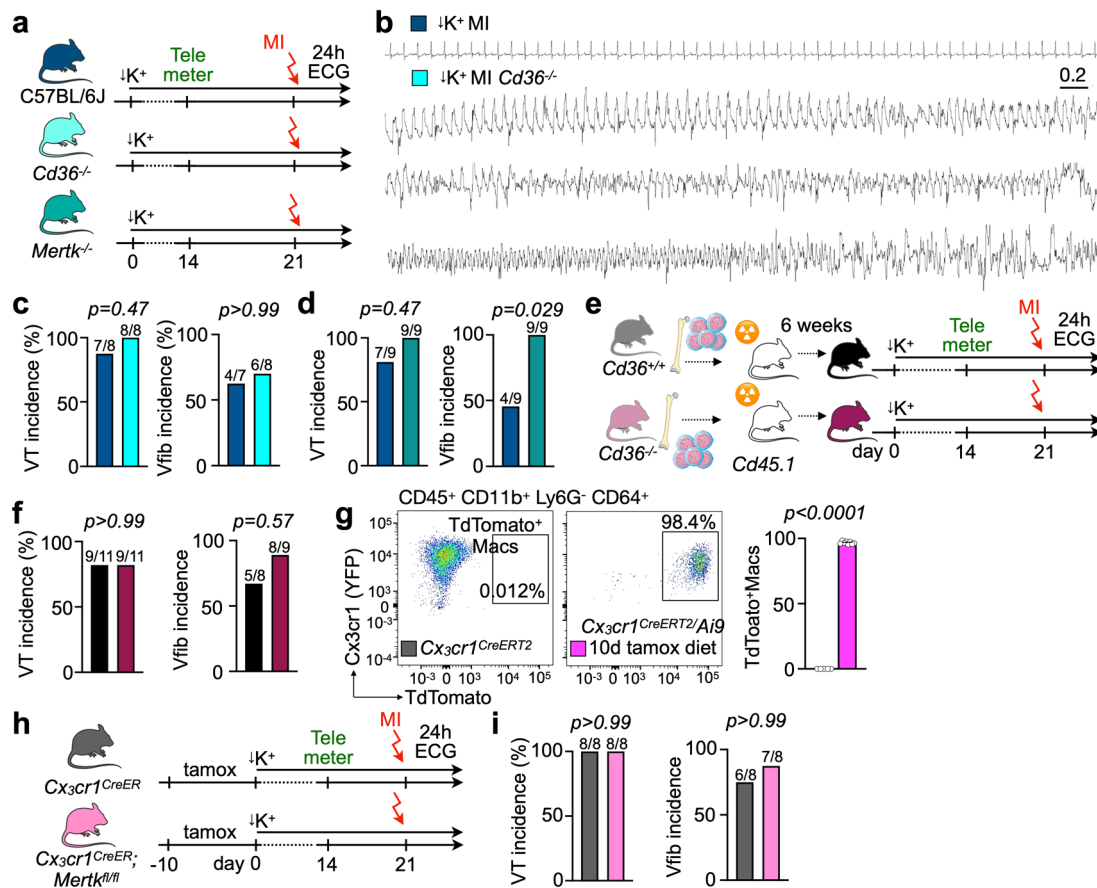
Extended Data Fig. 4 | Myeloid cell ablation and steady-state cardiac function. **a**, Experimental outline. **b**, Flow plots and quantification of cardiac macrophages in hypokalemic ($n=5$ mice) and hypokalemic mice undergoing macrophage depletion by Csf1Ri ($n=5$). Two-sided Mann Whitney test were used. **c**, Serum potassium in hypokalemic ($n=6$ mice) and Csf1Ri-treated hypokalemic mice ($n=7$). Two-sided unpaired t tests were used. **d**, Systolic function by echocardiography in hypokalemic ($n=6$ mice) and Csf1Ri treated hypokalemic mice ($n=6$). Two-sided unpaired t tests were used (except for heart rate, two-sided Mann Whitney test). **e**, Diastolic function by echocardiography in hypokalemic ($n=6$ mice, except E/e' : $n=5$) and Csf1Ri treated hypokalemic mice ($n=6$). Ratio between mitral inflow velocity and mitral valve annular early diastolic velocity, E/e' ; late diastolic trans-mitral flow velocity, E/A; global longitudinal peak strain, GLS. Two-sided unpaired t tests were used. **f**, Caspase 3, Fadd, Mlk1 and Tradd expression measured by quantitative PCR in hypokalemic ($n=4$ or $n=6$ mice, respectively) and Csf1Ri treated hypokalemic mice ($n=4$ or $n=6$ mice, respectively). Data from macrophage depletion group was normalized to data from hypokalemic mice. Two-sided unpaired t tests were used (except Mlk1 and Tradd, Mann Whitney test). **g**, Ventricular tachycardia (VT) inducibility and ventricular effective refractory period in an invasive electrophysiological study in hypokalemic ($n=7$ mice) and Csf1Ri treated hypokalemic mice ($n=5$). Fischer's exact test (VT inducibility) and unpaired t test were used (ventricular effective refractory period). **h**, VT inducibility and ventricular effective refractory period in an invasive electrophysiological study in hypokalemic ($n=8$ mice) and Ccr2^{-/-} treated hypokalemic mice ($n=10$). Fischer's exact test (VT inducibility) and unpaired t test were used (ventricular effective refractory period). **i**, VT incidence and Vfib incidence in C57BL/6 mice treated with Csf1Ri and undergoing STORM ($n=18$ mice) or hypokalemia ($n=9$). ECG recordings are from ambulatory mice for 24 hrs. Two-sided Fischer's exact tests were used. **j**, Ventricular tachycardia (VT) incidence and ventricular fibrillation (Vfib) incidence in Ccr2^{-/-} mice undergoing STORM ($n=20$ mice) or hypokalemia ($n=8$). ECG recordings are from ambulatory mice for 24 hrs. Two-sided Fischer's exact tests were used. Data are mean \pm SEM.



Extended Data Fig. 5 | Electrophysiological effects of myeloid cell ablation in mice. **a**, Experimental outline for macrophage depletion by feeding Csf1Ri PLX5622 via potassium-deficient diet in STORM mice. **b**, Flow plots and quantification of neutrophils (PMN) in STORM mice ($n=5$ mice) and mice undergoing Csf1Ri macrophage depletion ($n=7$). A two-sided Mann Whitney test was used. **c**, Infarct size, heart-weight-to-body-weight ratio and heart-weight-to-tibia-length ratio in STORM mice ($n=6$ or $n=8$ mice, respectively) and macrophage-depleted STORM mice ($n=5$ or $n=14$, respectively). All measurements were done 24hrs post MI. Two-sided unpaired t tests were used. **d**, Ventricular tachycardia (VT) incidence and ventricular fibrillation (Vfib) incidence from telemetric ECG recordings in ambulatory STORM mice ($n=11$ mice) and macrophage-depleted STORM mice ($n=12$). Two-sided Fischer's exact tests were used. **e**, Experimental outline for wild type C57BL/6J and Ccr2^{-/-} mice undergoing STORM procedure. **f**, Flow plots and quantification of neutrophils (PMN) in C57BL/6J STORM mice ($n=8$) and Ccr2^{-/-} STORM mice ($n=9$). Two-sided unpaired t tests were used. **g**, Infarct size, heart-weight-to-body-weight ratio and heart-weight-to-tibia-length ratio in C57BL/6J STORM mice ($n=6$ or $n=10$ mice, respectively) and Ccr2^{-/-} STORM mice ($n=7$ or $n=20$, respectively). All measurements were done 24hrs post MI. Two-sided unpaired t tests and Mann Whitney test (heart-weight-to-body-weight ratio) were used. **h**, VT incidence and Vfib incidence obtained by telemetric ECG-recordings in ambulatory C57BL/6J STORM mice ($n=11$ mice) and Ccr2^{-/-} STORM mice ($n=12$). Two-sided Fischer's exact tests were used. **i**, QT and QTc intervals in STORM mice ($n=10$ mice) and STORM mice with Csf1Ri ($n=6-7$). Two-sided unpaired t test was used. **j**, QT and QTc intervals in C57BL/6J STORM mice ($n=10$ mice) and Ccr2^{-/-} STORM mice ($n=7$). Two-sided unpaired t test was used. **k**, Kaplan-Meier survival curves of C57BL/6 STORM mice ($n=32$ mice), Ccr2^{-/-} STORM mice ($n=21$) and Csf1Ri STORM mice ($n=19$). A log-rank Mantel-Cox test was used. Data are mean \pm SEM.



Extended Data Fig. 6 | Mitochondrial health after myeloid cell ablation. **a**, Electron microscopy. Arrows indicate mitochondria. Scale bar indicates 600 nm. Experiment was repeated independently three times. **b**, Mitochondrial area and cristae formation in naive C57BL/6 (n=83 mitochondria (left) or n=16 (right), n=1 mouse) and mice undergoing STORM model (n=178 (left) or n=80 (right), n=3 mice, 5 FOVs/mouse). Dots are mitochondria. Two-sided Mann Whitney test (area) and two-sided unpaired t test (cristae) were used. **c**, Experimental outline. **d**, Incidence of paracrystalline inclusions in C57BL/6, Csf1R $^{-/-}$ and Ccr2 $^{-/-}$ STORM mice (mouse numbers are indicated in plots). Two-sided unpaired t tests were used. **e**, Exopher containing mitochondria in the extracellular space in the infarct of STORM mice. Scale bar indicates 2 μm or 800 nm. Experiment was repeated independently three times. **f**, Phagocyte with mitochondrial content in the infarct of STORM mouse. Scale bar indicates 600 nm or 200 nm and 1 μm or 400 nm. Experiment was repeated independently three times. **g**, Histological DAPI, mTmG/myh6-GFP, Mac3 and Tom20 staining from infarcts. Circles indicate area of interest. Scale bar indicates 5 μm . Experiment was repeated independently three times. **h**, Experimental outline. **i**, Mitochondrial count per field of view (FOV) in C57BL/6 (n=15 FOV), mice with Csf1R $^{-/-}$ (n=15) and Ccr2 $^{-/-}$ mice (n=15). n=3 mice/group, 5 FOVs/mouse. Nested t tests were used. **j**, Mitochondrial area in wild type mice (n=80 mitochondria), mice after Csf1R $^{-/-}$ (n=72) and Ccr2 $^{-/-}$ mice (n=66). n=3 mice/group; 5 FOVs/mouse. Dots are mitochondria. Two-sided Mann Whitney tests were used. **k**, Percent of cristae area per mitochondrial area in hearts of wild type mice (n=80 mitochondria), mice after Csf1R $^{-/-}$ (n=72) and Ccr2 $^{-/-}$ mice (n=66). n=3 mice/group; 5 FOVs/mouse. Dots are mitochondria. Two-sided Mann Whitney tests were used. **l**, Experimental outline. **m**, Fluorescence images from cardiac short axis slices after injection of PBS or FCCP. Target-to-background ratio (TBR) from FRI. Background mean fluorescence intensity: image background outside tissue. PBS (n=3 mice) and FCCP (n=4 mice). Dots are cardiac slices. Unpaired t test was used. **n**, Experimental outline. **o**, TBR from FRI. Background fluorescence intensity was measured in image backgrounds. Control mice (n=18 images), mice treated with Csf1R $^{-/-}$ (n=18 images) and Ccr2 $^{-/-}$ mice (n=17 images), all without MI. n=3 mice/group. Dots are cardiac slices. Two-sided unpaired t test was used. Data are mean \pm SEM.



Extended Data Fig. 7 | Scavenger receptor deletion facilitates post-MI ventricular. **a**, Experimental outline for C57BL/6 controls, *Cd36*^{-/-} and *Mertk*^{-/-} mice, all undergoing STORM. **b**, ECG tracing from a *Cd36*^{-/-} mouse experiencing sustained ventricular tachycardia (VT) transforming into ventricular fibrillation (Vfib) and leading to sudden cardiac death shortly after MI induction. **c**, VT incidence and Vfib incidence (mouse numbers in plots) from telemetric ECG recordings in ambulatory C57BL/6 STORM mice ($n=7$ mice) and *Cd36*^{-/-} STORM mice ($n=8$). Two-sided Fisher's exact tests were used. **d**, VT incidence and Vfib incidence (mouse numbers in plots) from telemetric ECG recordings in ambulatory C57BL/6 STORM mice ($n=9$ mice) and *Mertk*^{-/-} STORM mice ($n=9$). Two-sided Fisher's exact tests were used. **e**, Experimental outline for bone marrow transplantation using wild type *Cd36*^{+/+} or *Cd36*^{-/-} donor mice. Lethally irradiated recipients were *Cd36*^{+/+} mice that subsequently underwent STORM. **f**, VT incidence and Vfib incidence (mouse numbers in plots) from telemetric ECG recordings in ambulatory *Cd36*^{+/+} control bone marrow chimeras ($n=8$ mice) and *Cd36*^{-/-} bone marrow chimeras ($n=9$) after STORM procedure. Two-sided Fisher's exact tests were used. **g**, Flow plots demonstrating Cre activity in resident cardiac macrophages of *Cx3cr1*^{CreERT2/Ai9} mice after consuming tamoxifen diet for 10 days. Unpaired t-test was used. **h**, Experimental outline. *Cx3cr1*^{CreER}; *Mertk*^{fl/fl} mice and *Cx3cr1*^{CreER} control mice were fed with tamoxifen (tamox)-containing diet for 10 days. **i**, VT incidence and Vfib incidence (mouse numbers in plots) from telemetric ECG recordings in ambulatory *Cx3cr1*^{CreER} controls and *Cx3cr1*^{CreER}; *Mertk*^{fl/fl} mice after STORM procedure. Two-sided Fisher's exact tests were used. Data are mean \pm SEM.

Extended Data Table 1 | Patient characteristics of Oxford cohort. Baseline characteristics of patients with MI with ST segment elevation (STEMI) and treated with PCI entering OxAMI study between June 2012 and March 2020 and meeting study inclusion and exclusion criteria. Data are presented as median with interquartile range (IQR) or n (%).

Demographics	n=217 patients
Age (years)	60 [52, 68]
Male gender (n, %)	189 (87%)
Coronary risk factors	
Hypertension (n, %)	77 (35%)
Diabetes (n, %)	22 (10%)
Previous MI (n, %)	14 (6%)
Smoking history (n, %)	68 (31%)
Family history (n, %)	55 (25%)
Pre-existing medications	
Beta-blockers (n, %)	8 (4%)
ACE inhibitor/ARB (n, %)	15 (7%)
Statin (n, %)	15 (7%)
Vital signs	
Systolic BP (mmHg)	130 [113, 145]
Diastolic BP (mmHg)	78 [67, 88]
Heart rate (bpm)	74 [66, 87]
Culprit coronary artery	
LAD (n, %)	102 (47%)
LCx (n, %)	30 (14%)
RCA (n, %)	80 (37%)
Other (n, %)	4 (1%)
PCI procedure	
Ischemic time (minutes)	178 [122, 272]
Number of stents	1 [1, 1]
Stent length (mm)	25 [17, 32]
Stent diameter (mm)	3.5 [3, 4]
Blood tests	
White cell count ($\times 10^9$ /L)	11.1 [8.9, 13.3]
Neutrophil count ($\times 10^9$ /L)	8.3 [6.7, 10.7]
Monocyte count ($\times 10^9$ /L)	0.9 [0.7, 1.2]
Peak troponin (ng/L)	42100 [9895, 50000]
Creatinine (mg/dL)	0.81 [0.70, 0.94]
CMR scan (48 hours)	
LV end diastolic volume (mL)	161 [132, 186]
LV ejection fraction (%)	48 [42, 53]
RV end diastolic volume (mL)	131 [107, 152]
RV ejection fraction (%)	57 [50, 62]
Area-at-risk (T1 mapping), %	39 [30, 51]
Infarct size (late gadolinium enhancement >5SD, %LV)	21 [12, 33]

Extended Data Table 2 | Patient characteristics of Mass General Brigham cohort. Baseline characteristics of patients undergoing treatment for acute MI (including STEMI and NSTEMI) at Massachusetts General Hospital between June 2015 and June 2020 and meeting study inclusion and exclusion criteria. Data are presented as median and interquartile range (IQR) or n (%).

Demographics	n=795 patients
Age (years)	68 [60, 75]
Male gender (n, %)	528 (66%)
Ethnicity	
Black or African American	49 (6%)
Asian	33 (4%)
White or caucasian	616 (77%)
Hispanic/Latino	3 (0.4%)
Other/unavailable	94 (12%)
MI type	
STEMI diagnosis	186 (23%)
NSTEMI diagnosis	609 (77%)
Blood tests	
Peak troponin (ng/L)	599 [150, 1935]
White cell count ($\times 10^9$ /L)	10.0 [7.4, 13.8]
Neutrophil count ($\times 10^9$ /L)	6.6 [4.7, 9.8]
Monocyte count ($\times 10^9$ /L)	0.8 [0.6, 1.1]
Basophil count ($\times 10^9$ /L)	0.04 [0.02, 0.05]
Creatinine (mg/dL)	1.2 [0.9, 1.8]

Extended Data Table 3 | Cox models for Mass General Brigham cohort. Association between peak neutrophil count (dichotomized at the median) and the composite outcome of death or cardiac arrest at 30 days in patients with acute MI as determined by Cox proportional hazard models. An unadjusted and a series of adjusted analyses in which the relevant and available covariates were progressively incorporated were performed. The performance of each model was evaluated by calculating the Akaike information criterion (AIC) and Bayesian information criterion (BIC). Model 3 provided the lowest values for both, indicating better performance. The neutrophil count remained associated with the risk of 30-day death or cardiac arrest in all conditions trialed.

Groups dichotomized at the median neutrophil count					
Model	Group	HR (95% CI)	P value	AIC	BIC
Unadjusted	Neutrophils < 6.6x10 ⁹ /L	Reference		950.3	953.2
	Neutrophils ≥ 6.6x10 ⁹ /L	4.5 (2.5, 8.1)	<0.001		
Model 1	Neutrophils < 6.6x10 ⁹ /L	Reference		941.0	949.5
	Neutrophils ≥ 6.6x10 ⁹ /L	4.5 (2.5, 8.1)	<0.001		
Model 2	Neutrophils < 6.6x10 ⁹ /L	Reference		937.8	952.0
	Neutrophils ≥ 6.6x10 ⁹ /L	4.1 (2.3, 7.6)	<0.001		
Model 3	Neutrophils < 6.6x10 ⁹ /L	Reference		722.5	745.2
	Neutrophils ≥ 6.6x10 ⁹ /L	3.9 (1.9, 8.0)	<0.001		
Model 1: age, gender					
Model 2: age, gender, peak troponin, STEMI diagnosis					
Model 3: age, gender, peak troponin, STEMI diagnosis, peak monocyte count, peak basophil count, peak creatinine					

Corresponding author(s): Matthias Nahrendorf

Last updated by author(s): 12/15/21

Reporting Summary

Nature Portfolio wishes to improve the reproducibility of the work that we publish. This form provides structure for consistency and transparency in reporting. For further information on Nature Portfolio policies, see our [Editorial Policies](#) and the [Editorial Policy Checklist](#).

Statistics

For all statistical analyses, confirm that the following items are present in the figure legend, table legend, main text, or Methods section.

n/a Confirmed

- The exact sample size (n) for each experimental group/condition, given as a discrete number and unit of measurement
- A statement on whether measurements were taken from distinct samples or whether the same sample was measured repeatedly
- The statistical test(s) used AND whether they are one- or two-sided
Only common tests should be described solely by name; describe more complex techniques in the Methods section.
- A description of all covariates tested
- A description of any assumptions or corrections, such as tests of normality and adjustment for multiple comparisons
- A full description of the statistical parameters including central tendency (e.g. means) or other basic estimates (e.g. regression coefficient) AND variation (e.g. standard deviation) or associated estimates of uncertainty (e.g. confidence intervals)
- For null hypothesis testing, the test statistic (e.g. F , t , r) with confidence intervals, effect sizes, degrees of freedom and P value noted
Give P values as exact values whenever suitable.
- For Bayesian analysis, information on the choice of priors and Markov chain Monte Carlo settings
- For hierarchical and complex designs, identification of the appropriate level for tests and full reporting of outcomes
- Estimates of effect sizes (e.g. Cohen's d , Pearson's r), indicating how they were calculated

Our web collection on [statistics for biologists](#) contains articles on many of the points above.

Software and code

Policy information about [availability of computer code](#)

Data collection	Flow cytometry data were acquired on an LSRII flow cytometer equipped with FACS Diva 6.1 software (BD Biosciences, San Jose, CA, USA). Light microscopy images were captured on a NanoZoomer 2.0RS (Hamamatsu, Shizuoka, Japan). Immunofluorescence images were taken with a Nikon 80i (Nikon, Tokyo, Japan). qPCR data were acquired on a 7500 Real-Time PCR system (Applied Biosystems, Foster City, CA, USA). Confocal microscopy was executed with an FV1000-MPE microscope and IV10-ASW 01.01.00.05 software (Olympus, Tokyo, Japan). telemetric recordings and EP studies were done using a PowerLab station (ADInstruments, Sydney, Australia) and Labchart 8 software DSI, St. Paul, MN, USA). Echocardiographic images were acquired using a Vevo® 3100 high-resolution Imaging System (FUJIFILM VisualSonics, Toronto, ON, Canada). Fluorescent reflectance imaging was carried out using epifluorescence microscope OV-110 (Olympus, Tokyo, Japan) or Sapphire Biomolecular Imager (Azure Biosystems, Dublin, Ca, USA).
Data analysis	Flow cytometry data were analyzed with FlowJo 10 software (BD, Franklin Lakes, NJ, USA). Immunofluorescence images, TEM images, Confocal microscopy images and FRI images were analyzed using ImageJ 1.8.0_172. Pseudo rainbow color schemes of FRI exemplary images were generated using OsiriX Lite software v.12.5.2 (Pixmeo SARL, CHE). Telemetric recordings were analyzed using Labchart 8 software DSI, St. Paul, MN, USA). Echocardiographic images were analyzed using VevoLab 3.0 and VevoStrain 2.0 (both FUJIFILM VisualSonics, Toronto, ON, Canada). GraphPad Prism 9 software (GraphPad, San Diego, CA, USA), IBM SPSS for Macintosh version 28.0.0.0 (Version 27.0. Armonk, NY: IBM Corp) and RStudio version 1.4.1717 (RStudio: Integrated Development for R, RStudio, Inc., Boston, MA) were used for statistical analysis.

For manuscripts utilizing custom algorithms or software that are central to the research but not yet described in published literature, software must be made available to editors and reviewers. We strongly encourage code deposition in a community repository (e.g. GitHub). See the Nature Portfolio [guidelines for submitting code & software](#) for further information.

Data

Policy information about [availability of data](#)

All manuscripts must include a [data availability statement](#). This statement should provide the following information, where applicable:

- Accession codes, unique identifiers, or web links for publicly available datasets
- A description of any restrictions on data availability
- For clinical datasets or third party data, please ensure that the statement adheres to our [policy](#)

scRNA-seq data are deposited in NCBI's Gene Expression Omnibus and are accessible through GEO Series accession number GSE157244.

Field-specific reporting

Please select the one below that is the best fit for your research. If you are not sure, read the appropriate sections before making your selection.

Life sciences Behavioural & social sciences Ecological, evolutionary & environmental sciences

For a reference copy of the document with all sections, see nature.com/documents/nr-reporting-summary-flat.pdf

Life sciences study design

All studies must disclose on these points even when the disclosure is negative.

Sample size	Sample size was approximated and derived from extensive publications within the cardiovascular field which are based on previous a priori power testing. No statistical methods were used to pre-determine sample sizes but our sample sizes are in agreement with those reported in previous publications. ref 15, 25, 33.
Data exclusions	No data points were excluded.
Replication	Experiments were reproduced at least once to confirm the obtained results.
Randomization	Animals were randomly assigned to experimental groups. No in vitro experiments were done.
Blinding	Investigators were blinded in flow-sorting experiments, histological stainings and analyses, TEM sample processing and image acquisition and partly in telemetric ECG analyses. Blinding was not possible, when experiments involved surgical intervention in mice.

Reporting for specific materials, systems and methods

We require information from authors about some types of materials, experimental systems and methods used in many studies. Here, indicate whether each material, system or method listed is relevant to your study. If you are not sure if a list item applies to your research, read the appropriate section before selecting a response.

Materials & experimental systems

n/a	Involved in the study
<input type="checkbox"/>	<input checked="" type="checkbox"/> Antibodies
<input checked="" type="checkbox"/>	<input type="checkbox"/> Eukaryotic cell lines
<input checked="" type="checkbox"/>	<input type="checkbox"/> Palaeontology and archaeology
<input type="checkbox"/>	<input checked="" type="checkbox"/> Animals and other organisms
<input type="checkbox"/>	<input checked="" type="checkbox"/> Human research participants
<input checked="" type="checkbox"/>	<input type="checkbox"/> Clinical data
<input checked="" type="checkbox"/>	<input type="checkbox"/> Dual use research of concern

Methods

n/a	Involved in the study
<input checked="" type="checkbox"/>	<input type="checkbox"/> ChIP-seq
<input type="checkbox"/>	<input checked="" type="checkbox"/> Flow cytometry
<input checked="" type="checkbox"/>	<input type="checkbox"/> MRI-based neuroimaging

Antibodies

Antibodies used

Antibodies for flow cytometry:
 CD45-PerCP/Cy5.5 (clone 30-F11, 1:600, 103132, BioLegend), CD64-APC (clone X54-5/7.1, 1:600, 139305, BioLegend), Ly6G-PE/Cy7 (clone 1A8, 1:600, 127617, BioLegend), Ly6C-FITC (clone HK1.4, 1:600, 128006, BioLegend), CD11b-BV510 (clone M1/70, 1:600, 101245, BioLegend), CD115-BV605 (clone AFS98, 1:600, 135517, BioLegend), CD11b-APC (clone M1/70, 1:600, 101212, BioLegend), CD45-BV711 (30-F11, 1:600, 103147, BioLegend), CD3-APC/Cy7 (clone 17A2, 1:200, 100221, BioLegend), CD19-APC/Cy7 (clone 6D5, 1:300, 115529, BioLegend), B220-APC/Cy7 (clone RA3-6B2, 1:300, 103224, BioLegend), Nk1.1-APC/Cy7 (clone PK136, 1:300, 108724, BioLegend).

Antibodies for intravital microscopy:

anti-Ly6G-AF647 (10 µl diluted in 100 µl PBS, clone 1A8, 127610, BioLegend)

Antibody used for in vivo experiments:

anti-Ly6G (BE0075-1, BioXcell, West Lebanon, NH, USA), mouse IgG2a anti-rat antibody (BE0122, BioXcell, each 100 µg/d, i.p.), IgG2a isotype controls (BE0085 and BE0089, both BioXcell)

Validation

All antibodies used for flow and intravital microscopy were previously validated for the respective application by the distributor. Individual listings of citations (>5 for all listed antibodies) describe the use of these reagents in the imaging or cytometric application in which they were used on each antibody's manufacturer page which can be accessed using the catalog numbers provided above. Additionally, our laboratory has utilized this panel of intravital microscopy and flow cytometry antibodies in recent publications including (Vandoorne, Rohde D et al Circ Res 2018; 123 (4): 415-427). Validation of antibodies for in vivo experiments involving neutrophil depletion was performed by Boivin et al., 2020 (Boivin et al., Nat Commun. 2020 Jun 2;11(1):2762).

Animals and other organisms

Policy information about [studies involving animals](#); [ARRIVE guidelines](#) recommended for reporting animal research

Laboratory animals

The following mouse strains were used: Wild type C57BL/6J, tamoxifen-inducible B6J.B6N(Cg)-Cx3cr1tm1.1(cre)Jung/J (Cx3cr1CreERT2), B6.SJL-Ptprca Pepcb/BoyJ (Cd45.1), B6.129S4-Ccr2tm1Ifc/J (Ccr2-/-), B6.129P2-Lcn2tm1Aade/AkiJ (Lcn2-/-), B6.129S1-Cd36tm1Mfe/J (Cd36-/-), B6.129-Mertktnm1Grl/J (Mertk-/-) and B6.Cg-Gt(ROSA)26Sortm9(CAG-tdTomato)Hze/J (Ai9) mice were purchased from The Jackson Laboratory (Bar Harbor, ME, USA). Mertkfl/fl mice were kindly provided by Prof. Carla Rothlin (Yale University) {DeBerge et al., 2017, #157093}. B6.Cg-Tg(Myh6-GCaMP8)B4-10Mik/J (Myh6-GCaMP8) mice were kindly provided by Prof. Aaron Aguirre (Mass. General Hospital) (breeders received from Cornell Heart Lung Blood Resource for Optogenetic Mouse Signaling). Ly6G-Cre mice were kindly provided by Prof. Mikael Pittet (Mass. General Hospital) (breeders received from Institute for Experimental Immunology and Imaging, University Hospital Essen, Germany) and were bred to Ai9 mice in order to generate Ly6GTdtomato mice as reported previously {Hasenberg et al., 2015, #89518}. We used male and female mice with 8-20 weeks of age. Where appropriate, age- and sex-matched mice were used for experiments.

Wild animals

This study did not involve wild animals.

Field-collected samples

This study did not involve field-collected samples.

Ethics oversight

Animal protocols were approved by the Institutional Animal Care and Use Committee (IACUC) at Massachusetts General Hospital. All animal experiments were performed in compliance with relevant ethical regulations and all efforts were made to avoid suffering of animals.

Note that full information on the approval of the study protocol must also be provided in the manuscript.

Human research participants

Policy information about [studies involving human research participants](#)

Population characteristics

Oxford cohort

The Oxford cohort comprised 217 patients of whom 189 (87%) were male. The median age was 60 [IQR 52, 68].

Mass General Brigham cohort

The Mass General Brigham cohort comprised 795 patients of whom 528 (66%) were male. The median age was 68 [IQR 60, 75].

Recruitment

Oxford cohort

Patients with ST-segment elevation myocardial infarction (STEMI) who underwent primary percutaneous coronary intervention (PPCI) at Oxford University Hospitals NHS Foundation Trust were prospectively enrolled into the Oxford Acute Myocardial Infarction (OxAMI) study between 2010 and 2020. Patients were excluded if they had a late presentation with symptom duration >12 hours, cardiogenic shock, previous coronary artery bypass grafting, severe heart valve disease, contraindication to MRI, age > 85 years, diagnosis of sepsis/infection during the same hospital episode, or use of immunosuppressants. This yielded a final cohort size of n=217. Verbal assent at the time of PPCI was followed by informed written consent, before data and samples were analyzed. No financial compensation was offered for participation in the study, although study related travel expenses could be reimbursed. PPCI was performed according to contemporary international guidelines.

Mass General Brigham cohort

To investigate links between circulating neutrophil counts and clinical outcomes following myocardial infarction, human subject data were collected retrospectively from a patient cohort at Massachusetts General Hospital, using the Partners Healthcare Research Patient Data Registry and the Partners Healthcare Electronic Data Warehouse. The Partners Data Warehouse is linked to the Social Security Death Index, assuring a high degree of completeness of follow-up. The research protocol was approved by the Partners Healthcare Institutional Review Board and the need for individual informed consent was waived. No financial compensation was offered to participants. We collected data from hematological testing and clinical outcomes for Massachusetts General Hospital patients with a coded diagnosis of myocardial infarction over a 5-year period between June 2015-June 2020. All patients had at least 365 days follow-up. Inclusion criteria for the study were (1) coded diagnosis of myocardial infarction (either NSTEMI or STEMI), (2) serum troponin result (either standard or high-sensitivity

assay) greater than the upper limit of normal, (3) at least one valid white cell count with a white cell differential within 24 hours before or 48 hours after the first positive troponin result and (4) age 40-85 years. Patients were excluded if they had a coded diagnosis of sepsis or other significant infection during the same episode as the myocardial infarction. For patients with multiple valid neutrophil counts within the time range of interest, the maximum value was used for analyses.

Ethics oversight

Oxford cohort

The study complies with the Declaration of Helsinki and was given a favorable opinion by a local research ethics committee (REC: 10/H0408/24).

Mass General Brigham cohort

The study complies with the Declaration of Helsinki and was approved by the Partners Healthcare Institutional Review Board.

Note that full information on the approval of the study protocol must also be provided in the manuscript.

Flow Cytometry

Plots

Confirm that:

- The axis labels state the marker and fluorochrome used (e.g. CD4-FITC).
- The axis scales are clearly visible. Include numbers along axes only for bottom left plot of group (a 'group' is an analysis of identical markers).
- All plots are contour plots with outliers or pseudocolor plots.
- A numerical value for number of cells or percentage (with statistics) is provided.

Methodology

Sample preparation

To assess cardiac leukocyte cell populations, mice were anesthetized and flushed through the left ventricle with 10 mL of ice-cold PBS in order to remove intravascular blood. Whole hearts were excised to remove the atria from the ventricles. After harvest, ventricular tissue was minced into small pieces and subjected to enzymatic digestion using collagenase I (450 U/mL), collagenase XI (60 U/mL), DNase and hyaluronidase (60 U/mL) (all Sigma-Aldrich, St. Louis, MO, USA) for 1 hr at 37 °C under agitation. Next, a single-cell solution was achieved by filtering the cell suspension through a 40 µm cell strainer (Falcon, NY, USA) followed by a washing/centrifugation step.

Instrument

Flow cytometry data were acquired on an LSRII flow cytometer (BD Biosciences, San Jose, CA, USA).

Software

FACS Diva 6.1 software (BD Biosciences, San Jose, CA, USA) was used for data collection. Data were analyzed with FlowJo 10 software (BD, Franklin Lakes, NJ, USA).

Cell population abundance

Purity of sorted cells was >95% as assessed by confirmatory flow cytometry.

Gating strategy

All cell populations were pre-gated on viable and single cells. Cardiac macrophages were identified as CD45+ CD11b+ Ly6G-Ly6Clow/int CD64+. Monocytes were identified as CD45+ CD11b+ Ly6G- Ly6Chigh. Neutrophils were identified as CD45+ CD11b+ Ly6G+. For neutrophil-depleted mice, neutrophils were identified using the following alternative gating strategy CD45+ CD11b+ Ly6Cint Cx3Cr1- SChi and monocytes were identified as CD45+ CD11b+ Cx3Cr1+ Ly6Chigh. In Ly6GTdTomato mice TdTomato+ macrophages and TdTomato+ monocytes were identified using the standard gating strategy as explained above and additionally gated on TdTomato+ to identify active phagocytosis of TdTomato+ neutrophils by monocytes and macrophages.

- Tick this box to confirm that a figure exemplifying the gating strategy is provided in the Supplementary Information.